Ore Geology Reviews 139 (2021) 104551

Contents lists available at ScienceDirect

Ore Geology Reviews

journal homepage: www.elsevier.com/locate/oregeorev

Ore genesis and fluid evolution of the Sandaozhuang supergiant W-Mo skarn deposit, southern margin of the North China Craton: Insights from scheelite, garnet and clinopyroxene geochemistry

Qiang Zhan [a,b,c], Xin-Yu Gao [d], Lei Meng [e], Tai-Ping Zhao [a,c,*]

[a] Key Laboratory of Mineralogy and Metallogeny, Guangzhou Institute of Geochemistry, Chinese Academy of Sciences, Guangzhou 510640, China
[b] University of Chinese Academy of Sciences, Beijing 100039, China
[c] CAS Center for Excellence in Deep Earth Science, Guangzhou 510640, China
[d] Guangdong Polytechnic of Water Resources and Electric Engineering, Guangzhou 510635, China
[e] State Key Laboratory of Ore Deposit Geochemistry, Institute of Geochemistry, Chinese Academy of Sciences, Guiyang 550081, China

ARTICLE INFO

Keywords:
Scheelite
Rare earth elements
Sr-Nd isotopes
the southern margin of the North China Craton
W-Mo skarn deposit

ABSTRACT

The Sandaozhuang deposit (0.55 Mt WO_3 at 0.112% and 0.75 Mt Mo at 0.109%), located in the southern margin of the North China Craton, is one of the largest W-Mo deposits in the world. This study carried out in-situ elemental analyses on skarn minerals, as well as elemental and Sr-Nd isotopic analyses on scheelites from the deposit, to constrain the metal source and fluid evolution of the deposit. Three generations of scheelite (Sch A to C) were identified based on petrographic observations, including prograde skarn and diopside-plagioclase hornfels-hosted Sch A, retrograde skarn-hosted Sch B, and quartz vein-hosted Sch C. Varieties of REE patterns in the scheelite are mainly controlled by different substitution mechanisms and crystallization of REE-enriched skarn minerals. The Mo contents decrease from early generation Sch A (1.57–24.45%) to Sch B (0.19–1.52%) and finally to Sch C (0.20–0.97%), and Eu anomalies of scheelite change from negative to positive and then back to negative values. The Sandaozhuang deposit is characterized by Mg-rich clinopyroxene ($Di_{40-81}Hd_{17-47}$), and grossularite–andradite ($And_{22-89}Gro_{6-77}$), similar to well-studied oxidized W skarn deposits worldwide, but the andradite contents of one garnet grain in the late prograde stage, decrease from the core (84.09%) to rim (75.12%). Composition changes of scheelite and garnet indicate that the ore-forming fluids changed from oxidized to reduced state in the skarn stage then to oxidized state in the quartz-sulfide stage, and the variations in redox state favoured the muti-stage Mo mineralization. The relatively uniform Y/Ho ratios of the Nannihu granite porphyry and scheelite imply that the ore-forming fluids are mainly derived from the porphyry. Scheelites from Sandaozhuang are characterized by low $\varepsilon_{Nd}(t)$ values (−14.7 to − 11.8), which are consistent with those for the Nannihu granite porphyry. Such a coincidence indicates that ore-forming fluids were mainly derived from the ore-hosting porphyry. However, the initial $^{87}Sr/^{86}Sr$ ratios of scheelites (0.7158–0.7295) are significantly higher than those of the Nannihu granite porphyry and other granites in the Luanchuan ore district (0.7047–0.7098), indicating that the Neoproterozoic Luanchuan Group with radiogenic Sr isotopic compositions contributed to tungsten mineralization, and the intense fluid-rock interaction between the ore-forming fluids derived from the granite porphyry and the Luanchuan Group country rocks may play an important role in tungsten mineralization.

1. Introduction

Scheelite ($CaWO_4$), one of the two main ore minerals of tungsten, is exploited mainly in skarn-type and porphyry-type deposits (Noble et al., 1984; Song et al., 2014; Mao et al., 2017; Li et al., 2019; Su et al., 2019; Liu et al., 2020). In addition, it is a common accessory mineral in quartz vein-type gold deposits (Bell et al., 1989; Voicu et al., 2000; Kempe et al., 2001; Xiong et al., 2006; Dostal et al., 2009). Rare earth elements (REEs), Sr, and Pb can easily enter the scheelite crystal structure where they substitute for Ca^{2+} due to the similar ionic radii and electronic

* Corresponding author at: Key Laboratory of Mineralogy and Metallogeny, Guangzhou Institute of Geochemistry, Chinese Academy of Sciences, Guangzhou 510640, China.
E-mail address: tpzhao@gig.ac.cn (T.-P. Zhao).

https://doi.org/10.1016/j.oregeorev.2021.104551
Received 19 March 2021; Received in revised form 17 October 2021; Accepted 28 October 2021
Available online 4 November 2021

configurations (Cottrant, 1981; Ghaderi et al., 1999). REE patterns of scheelite are used to define the mineralization conditions and the origin of ore-forming fluids (Tomschi et al., 1986; Guo et al., 2016; Brugger et al., 2008; Ding et al., 2018; Poulin et al., 2018; Liu et al., 2019). Sr content and Eu anomalies in scheelite record fluid-rock interactions and redox environment of the ore-forming fluids (Ghaderi et al., 1999; Song et al., 2014; Orhan, 2017; Poulin et al., 2018; Li et al., 2019; Sun et al., 2019; Yuan et al., 2019). Scheelite lattice can contain appropriate amount of Sm, Nd, and Sr but reject Rb, Sr and Nd isotopic characteristics of scheelite are widely used to trace the source and evolution of ore-forming fluids (Bell et al., 1989; Mueller et al., 1991; Kent et al., 1995; Eichhorn et al., 1997; Voicu et al., 2000; Song et al., 2014; Sun et al., 2019).

In the magmatic-hydrothermal W-Mo deposits, molybdenum is usually transported as oxidized Mo^{6+}. Scheelite can accommodate the Mo^{6+}, because Mo^{6+} can substitute for W^{6+} to form a complete, albeit non-ideal solid solution series between powellite ($CaMoO_4$) and scheelite ($CaWO_4$) (Hsu and Galli, 1973; Rempel et al., 2009; Song et al., 2014). In contrast, the reduced molybdenum (Mo^{4+}) deposits as molybdenite (Hsu and Galli, 1973; Poulin, 2016). Hence, the redox conditions must be changed during the process of Mo ore precipitation. Molybdenite and scheelite can precipitate under similar temperatures (Cao, 1989; Wood and Samson, 2000), but molybdenite was generally precipitated under the conditions of high fS_2 and low fO_2 (Poulin, 2016),

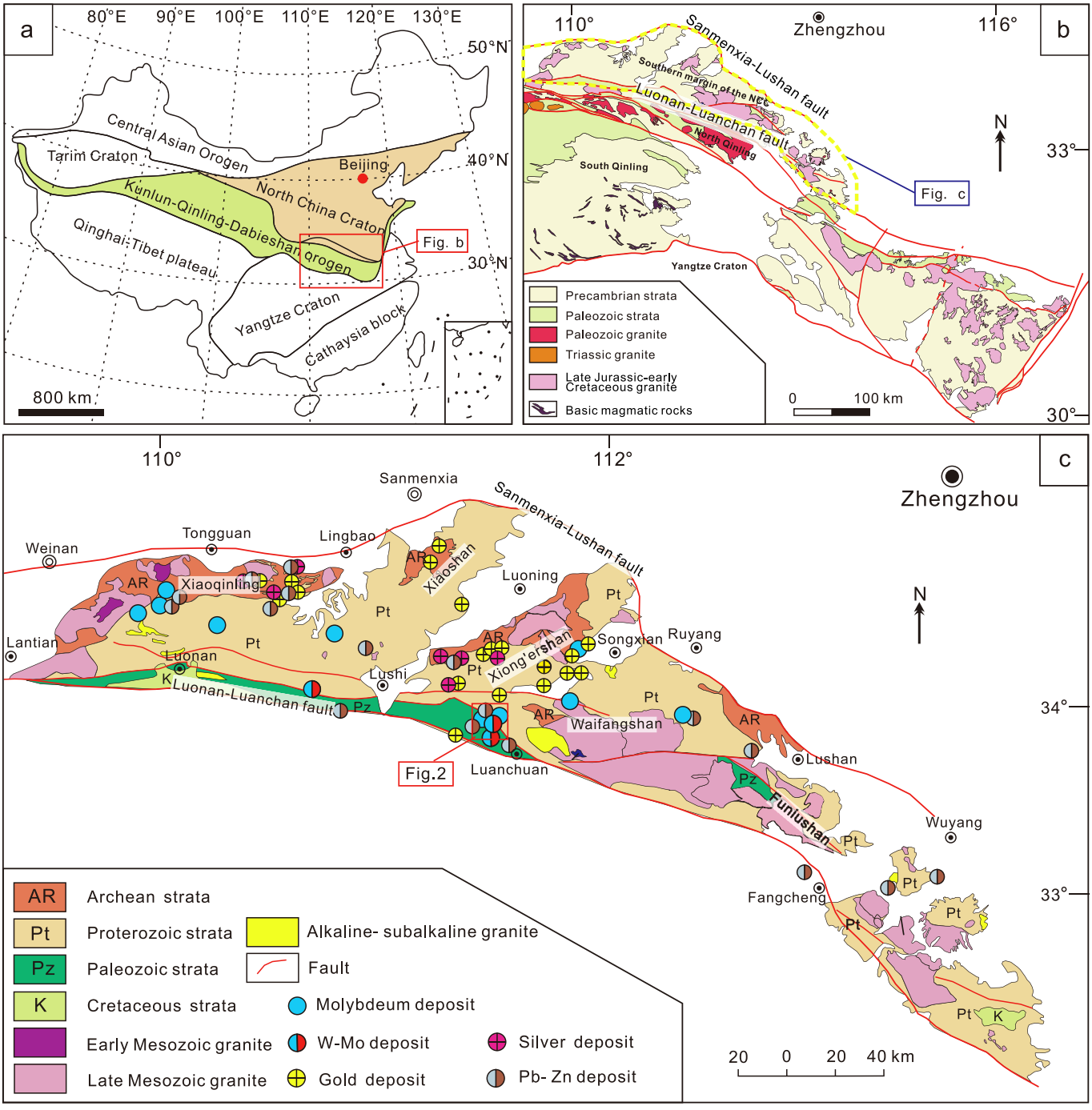

Fig. 1. (a) Location of the Qinling Orogenic Belt in the simplified tectonic map of China. (b) Simplified geological map of the Qinling Orogenic Belt (modified from Zhang et al., 1996). (c) Distribution of the Mesozoic granitoids and related ore deposits in the southern margin of the North China Craton.

and its solubility is a function of reduced sulfur concentration. In comparison, the precipitation of scheelite is little affected by the change of redox state (Polya, 1988). Therefore, scheelite can record the Mo mineralization process in the W-Mo skarn deposits (Liu et al., 2020). However, few studies have explored the complicated molybdenum mineralization process from the perspective of scheelite mineralogy.

Late Mesozoic granitoid intrusions and molybdenum gold polymetallic deposits are widely distributed in the southern margin of North China Craton (NCC) (Mao et al., 2008, 2010). The region is rich in Mo, Au, Ag, Pb, Zn and W resources, and is one of the most important metallogenic provinces in China (Chen et al., 2000; Mao et al., 2008; Li et al., 2012; Bao et al., 2014; Fig. 1). Extensive studies on the region have been conducted, however, most of the studies focused on molybdenum and gold mineralization. The fluid and metal source and metallogenic mechanism of the large-scale tungsten deposits in this region have not been fully explored. Tungsten mineralization in the south margin of NCC is only associated with large-scale and super large-scale skarn or porphyry-skarn molybdenum deposits. Major W-Mo deposits include the Sandaozhuang and Yuku deposits in the Luanchuan ore district, and the Yechangping deposit in the Lushi area (Xiao and Sun, 2007; Shi et al., 2009; Han et al., 2015; Fig. 1c).

The Sandaozhuang deposit, contains a resource of 0.75 Mt Mo grading average 0.109% Mo, and 0.55 Mt W grading average 0.112% WO_3, and is the largest W-Mo deposit in the southern margin of NCC. In addition, it is the largest Mo and third largest W skarn deposit in China (Chang et al., 2019). Scheelite with various Mo contents coexists with molybdenite in different mineralization stages (MoO_3 up to 24.5 wt%) at Sandaozhuang. Previous studies on the Sandaozhuang deposit mainly focus on geochronology and ore geology of molybdenum mineralization (Shi et al., 2009; Xiang et al., 2012a, 2012b; Bao et al. 2014). However, the fluid nature and ore-forming process of the Sandaozhuang deposit are still poorly understood.

The Sandaozhuang deposit provides a good opportunity for us to use the systematic geochemistry of scheelite, related garnet and clinopyroxene to investigate the effect of scheelite precipitation on the complicated molybdenum mineralization and constrain the genesis of the world's most typical W-Mo skarn deposit. In this study, we obtained in-situ major and trace elements, back-scattered electron (BSE) images, cathodoluminescence (CL) images and Sr-Nd isotopes for different types of scheelite from the Sandaozhuang deposit, with the purpose to provide insights into (1) the separation and precipitation mechanism of molybdenum and tungsten during ore-forming process, (2) the origin and ore-forming fluid evolution history.

2. Geological background

2.1. Regional geology

The southern margin of the NCC is bordered by the Luanchuan Fault to the south and the Sanmenxia-Lushan Fault to the north (Fig. 1b). Archean to Paleoproterozoic crystalline basement and the overlying late Paleoproterozoic to Phanerozoic unmetamorphosed sedimentary cover sequences are the main outcrop strata in this region. The crystalline basement is dominated by the Taihua complex (2.26–2.84 Ga), which is composed of amphibolite- to granulite-facies metamorphic rocks (Kröner et al., 1988; Bao et al., 2014; Jin et al., 2018). Furthermore, the crystalline basement is unconformably overlain by the late Proterozoic Xiong'er Group volcanic rocks (1.75–1.78 Ga) (Zhao et al., 2004). The Xiong'er Group is unconformably covered by the Meso-Neoproterozoic Guandaokou and Luanchuan groups, which consist of shore to shallow-marine facies carbonaceous carbonate, shale, chert and sandstone (Chen et al., 2004).

The Sandaozhuang W-Mo skarn deposit, located in the Luanchuan ore district of the southern margin of the NCC, is a member of the five super-large molybdenum deposits in the East Qinling molybdenum ore belt. The Sandaozhuang deposit, together with the Nannihu porphyry Mo deposit and the Shangfanggou porphyry-skarn Mo-Fe deposit, forms the world-famous Luanchuan Mo field (Yang et al., 2009; Fig. 2). The Mo orebodies of the Luanchuan Mo field is hosted in the Luanchuan Group, which is composed of the basal Baishugou, Sanchuan, Nannihu and upper Meiyaogou Formations in ascending sequence (Yang et al., 2012; Fig. 2). Hornification and skarnization occur in the Luanchuan Group due to Yanshanian magmatism (Shi et al., 2009). The NWW-trending Luanchuan fault is the most significant fault in the molybdenum ore field, which has undergone several brittle-ductile deformation in the Mesozoic orogenic process. A series of NNE- trending fault structures are superimposed on the Luanchuan fault in the later stage (Yang et al., 2012). Late Jurassic-early Cretaceous granites widely distributed in the Luanchuan molybdenum ore field are closely related to the regional super-large molybdenum mineralization in space and time. They occur as small stocks, dykes and veins at the intersection of NWW- trending faults and NNE- trending faults (Yang et al., 2009; Mao et al., 2011).

2.2. Deposit geology

The Nannihu-Sandaozhuang Mo-W system, located in the inner and outer contact zone of Nannihu granite porphyry, is hosted by the Sanchuan and Nannihu Formations of the Luanchuan Group (Yang et al., 2012). It is divided into two deposits, Nannihu and Sandaozhuang, based on the huge scale and different mineralization type (Fig. 3, Yang et al., 2009; Shi et al., 2009; Xiang et al., 2012b). The Nannihu deposit is dominated by molybdenum mineralization (0.65 Mt Mo at 0.06%). The Mo ore body is mainly hosted in the Nannihu granite porphyry and altered biotite felsic hornfels of the Nannihu Formation, and the ore structure is mainly veinlet (Fig. 3). In addition to molybdenum mineralization, large-scale tungsten mineralization occurs in Sandaozhuang deposit (0.75 Mt Mo at 0.109% and 0.55 Mt WO_3 at 0.112%) (Xiang et al., 2012a). Ore-bearing strata in the Sandaozhuang W-Mo skarn deposit are mainly calcareous schist with thin layer of marble in the upper part of the Sanchuan Formation of the Luanchuan Group. Calsilicate hornfels and skarns are formed after contact metamorphism and metasomatism. The ore type and structure are dominated by skarn type and disseminated structure, respectively. In addition, a variety of molybdenite-bearing quartz veins occur in skarn, diopside-plagioclase hornfels and felsic hornfels (Fig. 3). The main orebody which is composed of skarns and diopside-plagioclase hornfels at the Sandaozhuang deposit is about 1.5 km long from east to west and 1 km wide from south to north and extents slightly to the southwest.

The Nannihu granite porphyry covers an area of about 0.12 km^2, which transits from shallow porphyry monzogranite to deep porphyry biotite granodiorite. Zircon U–Pb ages of the Nannihu porphyritic monzogranite range from 145 to 157 Ma (Bao et al., 2009, 2014; Mao et al., 2010; Xiang et al., 2012a), and molybdenite from the deposits yield Re-Os ages of 140 to 156 Ma (Huang et al., 1995; Li et al., 2003; Mao et al., 2008; Xiang et al., 2012a). The porphyry body is mainly located in the Nannihu deposit (Fig. 3), and only a few are found in the deep part of Sandaozhuang mining area, whereas the endoskarn is rarely developed. The Sandaozhuang deposit is mainly characterized by wall rock hornification and skarn in the outer contact zone, therefore, it is generally determined as a skarn type deposit (Shi et al., 2009).

3. Sampling and analytical methods

In this study, several tungsten-bearing ore samples were collected from the Sandaozhuang open pit. Two samples (18SDZ-6 and 18SDZ-9) were collected from garnet-clinopyroxene-wollastonite skarns, eleven samples (18SDZ-12, −20, −26, −27, −29, −34, −35, −37, −38, −39 and − 40) from garnet-tremolite/actinolite-epidote skarns and two samples (18SDZ-55 and 18SDZ-58) were collected from diopside-plagioclase hornfels. Selected samples were prepared as polished thin sections for electron microscope, in situ electron probe and laser ablation-inductively coupled plasma-mass spectrometry (LA-ICP-MS)

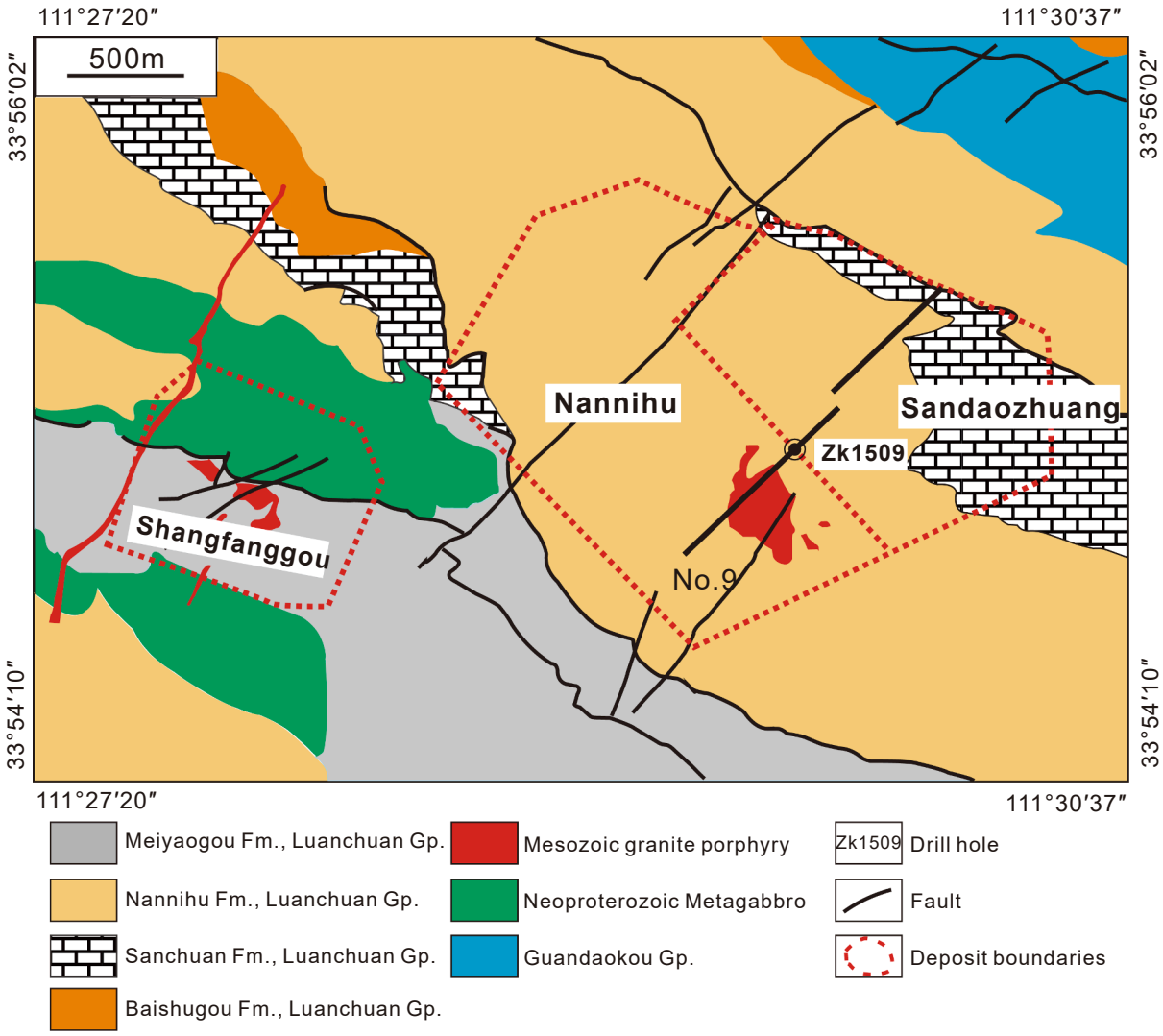

Fig. 2. Geological map of the Luanchuan Mo ore field (Modified from Yang et al., 2012).

analysis. Scheelite samples (SDZ-2, −4, −8, −17, −18, −29, −30 and −38) were collected from garnet skarns and diopside-plagioclase hornfels for Sr-Nd isotope analysis.

3.1. Scanning electron microscopes (SEM) and electron microprobe analysis (EMPA)

SEM-back-scattered electron (BSE) and SEM-Cathodoluminescence (CL) images of scheelite and skarn minerals were acquired to reveal the internal textures, using SEM (SUPRA 55 SAPPHIRE, ZEISS Company, Germany) at the State Key Laboratory of Isotope Chemistry, Guangzhou Institute of Geochemistry, Chinese Academy of Sciences.

Major elements of scheelite, garnet and clinopyroxene were determined by electron probe microanalysis (EPMA) using a JEOL JXA-8230 at the CAS Key Laboratory of Mineralogy and Metallogeny, Guangzhou Institute of Geochemistry, Chinese Academy of Sciences. All elements were analyzed under the operating conditions of 5 μ m beam current, 20nA probe current and 15 kV accelerating voltage. Peak and beak-ground counting times were 10 s and 5 s, respectively. Standards used for data correction were orthoclase for K, albite for Na, chrome-diopside for Si and Ca, olivine for Mg, magnetite for Fe, rutile for Ti, rhodonite for Mn, $ZnWO_4$ for W, molybdenite for Mo, Cr_2O_3 for Cr, jadeite for Al, apatite for P and $PbCrO_4$ for Pb.

3.2. In situ LA-ICP-MS trace element analysis

In situ trace element analysis of scheelite, garnet and clinopyroxene, was performed on polished thick sections using laser ablation inductively-coupled plasma mass spectrometry (LA-ICP-MS) at the In situ Mineral Geochemistry Lab, Ore Deposit and Exploration Centre (ODEC), Hefei University of Technology. Analyses were conducted on a Photon Machines Analyte HE 193 nm ArF Excimer Laser Ablation system coupled with an Agilent 7900 Quadrupole ICP-MS. After measuring the gas blank for 20 s, the uniform spot diameter of 30 μ m at 8 Hz with the energy of ~ 4 J/cm^2 were used for each analysis for 40 s. NIST 610 and BCR-2G were used as external standards to plot the calibration curve. CaO contents of scheelite and SiO_2 of garnet and clinopyroxene determined by EMPA were used as internal standards. The standard reference materials were run after every 10–15 unknowns and the detection limits for each element at each point of analysis were calculated. The Excel-based software ICPMSDataCal was used for offline data processing (Liu et al. 2008). The analytical accuracy for most measured trace elements was better than 8%, and the results were consistent with reference values within ± 10%.

Elemental mapping of scheelite was measured using a 193 nm ArF Excimer Laser Ablation system (NWR 193) coupled with a ThermoFisher iCAP RQ and a dual concentric injector (DCI) plasma torch integrated with two-volume ablation cell at the Tuoyan *in-situ* Analysis Lab

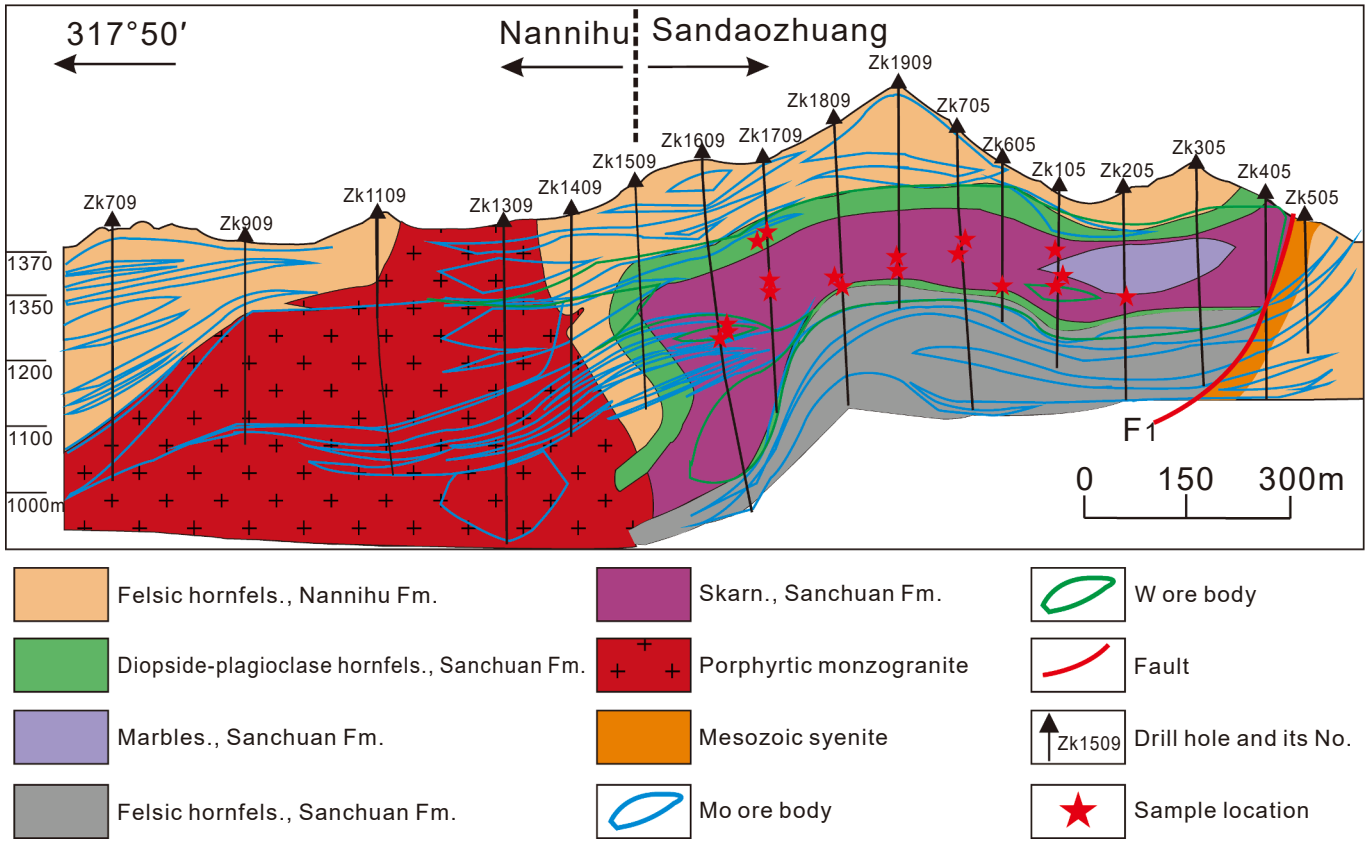

Fig. 3. Geological section along No. 9 exploration line of the Nannihu Mo ore field (Modified from Geological Survey Team 1 of Henan Bureau of Geology, 1980).

(Guangzhou, China). Ablation site was determined by line scanning pattern, and the raster image was composed of lines evenly arranged in chronological order. The ICP-MS was set to time-resolved method and was automatically triggered by laser. ^{43}Ca, ^{23}Na, ^{51}V, ^{55}Mn, ^{88}Sr, ^{93}Nb, ^{95}Mo, ^{183}W, ^{139}La, ^{140}Ce, ^{141}Pr, ^{146}Nd, ^{147}Sm, ^{153}Eu, ^{157}Gd, ^{159}Tb, ^{163}Dy, ^{165}Ho, ^{166}Er, ^{169}Tm, ^{172}Yb, ^{175}Lu and ^{238}U elements were collected at each duty cycle, with the dwell time set to at 6 ms for each element. NIST 610, NIST 612 and BCR-2G were added as standard reference materials at the beginning and end of the total scan line. The laser spot was set at 5 μ m, and there is no space between lines. Laser frequency and the laser scan speed were set at 100 Hz and 6 μm/s, respectively. The software Iolite (version 3.73) was used for analysis of images (Hellstrom et al., 2008; Paton et al., 2011).

3.3. Sr-Nd isotope analysis

Approximately 50 mg of scheelite samples were dissolved in Teflon bombs using a mixture of HNO_3 + HF + $HClO_4$ on an oven (190 ℃) for two days and dried on a hot plate at 150 ℃. 3 mL of 6 M HCl was added to the Teflon bombs and the mixture was evaporated to dryness. After drying, the samples were dissolved in 1 mL 2.5 M HCl. The solution was centrifuged, and the supernatant was loaded onto the pretreated resin column. Sm and Nd were separated by HEHEHP chromatographic columns. Sr and LREE were separated by 2 mL AG50W. Isotopic analyses were carried out at Tianjin Institute of Geology and Mineral Resources, China Geological Survey, using Thermo-Finnigan TRITON thermal ionization mass spectrometer (TIMS). Sr and Nd isotopic ratios were normalized against $^{86}Sr/^{88}Sr = 0.1194$ and $^{146}Nd/^{144}Nd = 0.7219$, respectively. Sr standard NBS-987 yielded $^{87}Sr/^{86}Sr = 0.710231 \pm 0.000012(2\sigma)$, and LRIG Nd standard gave $^{143}Nd/^{144}Nd = 0.512202 \pm 0.000003(2\sigma)$. Accuracy of separation and purification of Sr and Nd was determined by rock standard USGS BCR-2, which yielded $^{87}Sr/^{86}Sr = 0.705050 \pm 0.000005(2\sigma)$ and $^{143}Nd/^{144}Nd = 0.512624 \pm 0.000003$ (2σ).

4. Ore paragenesis

Four main mineralization stages were identified based on mineral assemblages and crosscutting relationship in the Sandaozhuang W-Mo deposit (Fig. 4). These stages included: (1) prograde skarn stage (clinoproxene-wollastonite-garnet-scheelite), (2) retrograde skarn stage (actinolite-fluorite-chlorite-epidote-scheelite-molybdenite), (3) quartz-sulfide stage (quartz-fluorite-molybdenite-pyrite vein with little tungsten mineralization), and (4) calcite stage (quartz-calcite vein with little molybdenum mineralization).

Prograde skarn stage: Porphyry bodies only occur in the deep part of the mining area, therefore, the endoskarn of the Sandaozhuang deposit is not developed. High-temperature prograde skarn stage is characterized by clinopyroxene, garnet and wollastonite. Disseminated fine grained scheelite, and few disseminated molybdenite were present in the garnet-pyroxene skarn (Fig. 5b-c, Fig. 6a-d) or the skarn bodies which occur as veins several centimeters to tens of centimeters wide in marble during this stage (Fig. 5a). Few disseminated fine scheelite grains occur in the diopside-plagioclase hornfels (Fig. 5h, Fig. 6e), which are mainly composed of anhydrous minerals, such as diopside, plagioclase, quartz and minor garnet. We also classify these scheelites grains into the prograde skarn stage, although they occur in cal-silicate hornfels, not the typical skarns.

Retrograde skarn stage: A large number of sulfides and hydrous skarn minerals precipitated during this stage. Retrograde minerals consist mainly of epidote, chlorite, actinolite and fluorite (Fig. 5d-f, Fig. 6f-j). These hydrous skarn minerals overprint the prograde stage mineral assemblages. Prograde minerals, such as garnet, were transformed into epidote (Fig. 6j), and clinopyroxene were transformed into actinolite (Fig. 6f and g). The retrograde stage is the most important period of simultaneous mineralization of molybdenum and tungsten. Molybdenite

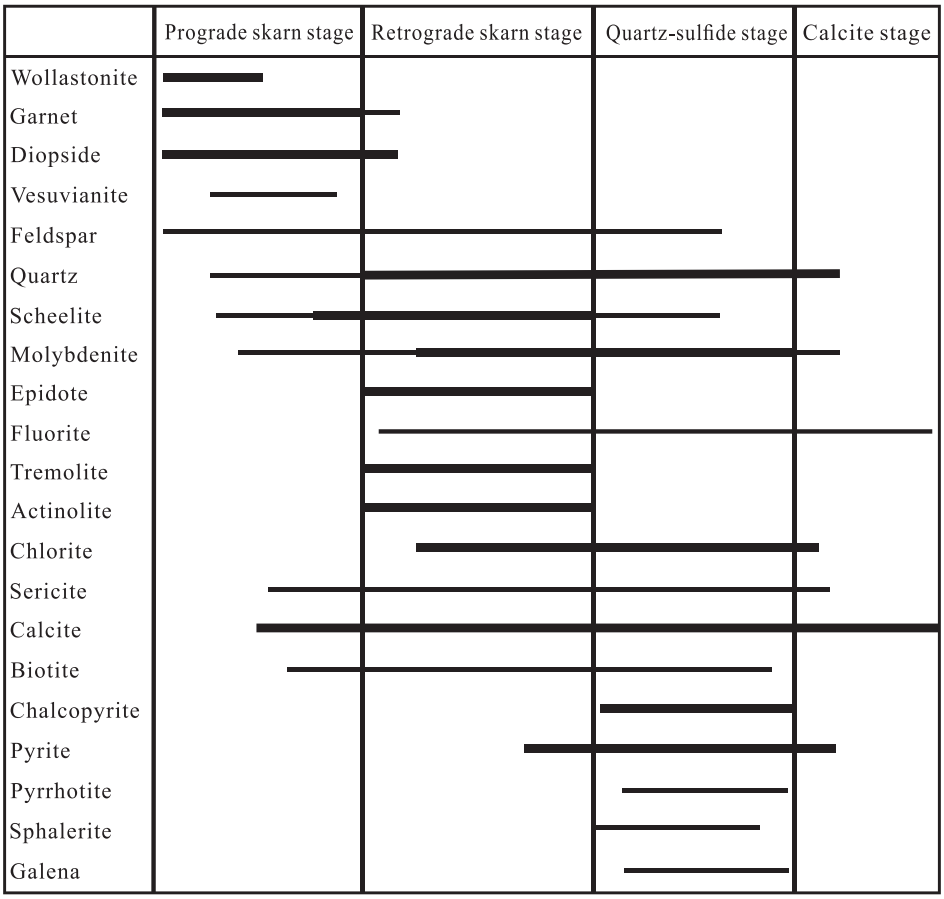

Fig. 4. Mineral paragenesis for the Sandaozhuang W-Mo deposit.

and scheelite commonly disseminate in the retrograde skarn ores and coexist with actinolite, fluorite and chlorite. It should be noted that the molybdenite always coexists closely with scheelite during the retrograde stage (Fig. 6f-i).

Quartz-sulfide stage and calcite stage: The quartz-sulfide stage is mainly characterized by molybdenum mineralization, with typical sulfide minerals, such as pyrite, sphalerite, chalcopyrite and minor pyrrhotite. These different sulfides, together with quartz, fluorite, potash feldspar and small amounts of biotite and calcite, form various types of quartz veins (Fig. 5e-h). Skarns, diopside-plagioclase hornfels and felsic hornfels are crosscut by these quartz- sulfide veins. Small amounts of scheelite are also observed in this stage (Fig. 5h, Fig. 6k and l), mainly euhedral, which coexist with quartz, pyrite, and calcite. These scheelite-bearing quartz veins mainly occur in the diopside-plagioclase hornfels and pyroxene skarn ores, indicating the importance of Ca produced by decomposition of plagioclase and pyroxene for vein-type tungsten mineralization in Sandaozhuang. Late calcite veins are composed of calcite, fluorite and minor quartz, which crosscut different ores and earlier quartz veins (Fig. 5i).

5. Results

5.1. BSE and CL images of scheelite

Scheelite in the Sandaozhuang deposit was grouped into three main generations based on BSE and CL characteristics and mineral paragenesis. Sch A precipitated in the prograde stage, based on the different occurrences, it can be further classified into Sch A-1, Sch A-2 and Sch A-3. Sch A-1 and Sch A-2 are characterized by dark domains in CL images (Fig. 7a and b), and coexist with clinopyroxene, garnet and wollastonite (Fig. 6a and d). Sch A-3 occurs in the form of disseminated fine grains in the diopside-plagioclase hornfels, and exhibits dark domains with homogeneous oscillatory zonation under CL imaging (Fig. 7c). BSE and CL images of Sch A-2 show dark inner domains, and mainly occur as cores crosscut or rimmed by Sch B, which comprise the lighter domains clearly formed later (Fig. 7d-g). The dark domains (Sch A-2) are either inhomogeneous, or show evidence of faint oscillatory zoning. Complex internal texture consisting of both CL-dark Sch A-2 and CL-bright Sch B zones is observed in an individual grain, which coexists with hydrous minerals and sulfides in the retrograde stage (Fig. 7d-g). Sch A-2 and Sch B represent the early and late generation scheelite, respectively. Sharp reaction fronts and close spatial relationship are observed between Sch A-2 and Sch B, with no change in shape of the primary crystals, and the pores and corrosion textures observed in Sch A-2 and Sch B (Fig. 7d-g), suggest a replacement process caused by the almost coeval occurrence of dissolution and reprecipitation. Notably, molybdenite always coexists with the Sch B in the retrograde stage (Fig. 7d-g). Sch C formed in the quartz-sulfide stage corresponds to the uniform bright region in BSE image, however, it exhibits homogeneous oscillatory zonation under CL (Fig. 7h and i).

5.2. Major and trace elements of scheelite

5.2.1. Major elements compositions

Composition of ten major elements was measured by electron probe microanalysis on twenty-nine scheelite grains from Sandaozhuang (Table. 1). Major compositions of different types of scheelite are wide (Fig. 8a). Scheelites from Sandaozhuang are generally high in Mo compared with vein-type W deposits and most skarn-type W deposits (Fig. 8b). Sch A contains high levels of Mo. Sch A-1 show high MoO_3 concentrations ranging from 1.57 to 2.23% with CaO from 20.40 to 20.91%, while Sch A-2 show significantly higher MoO_3 concentrations

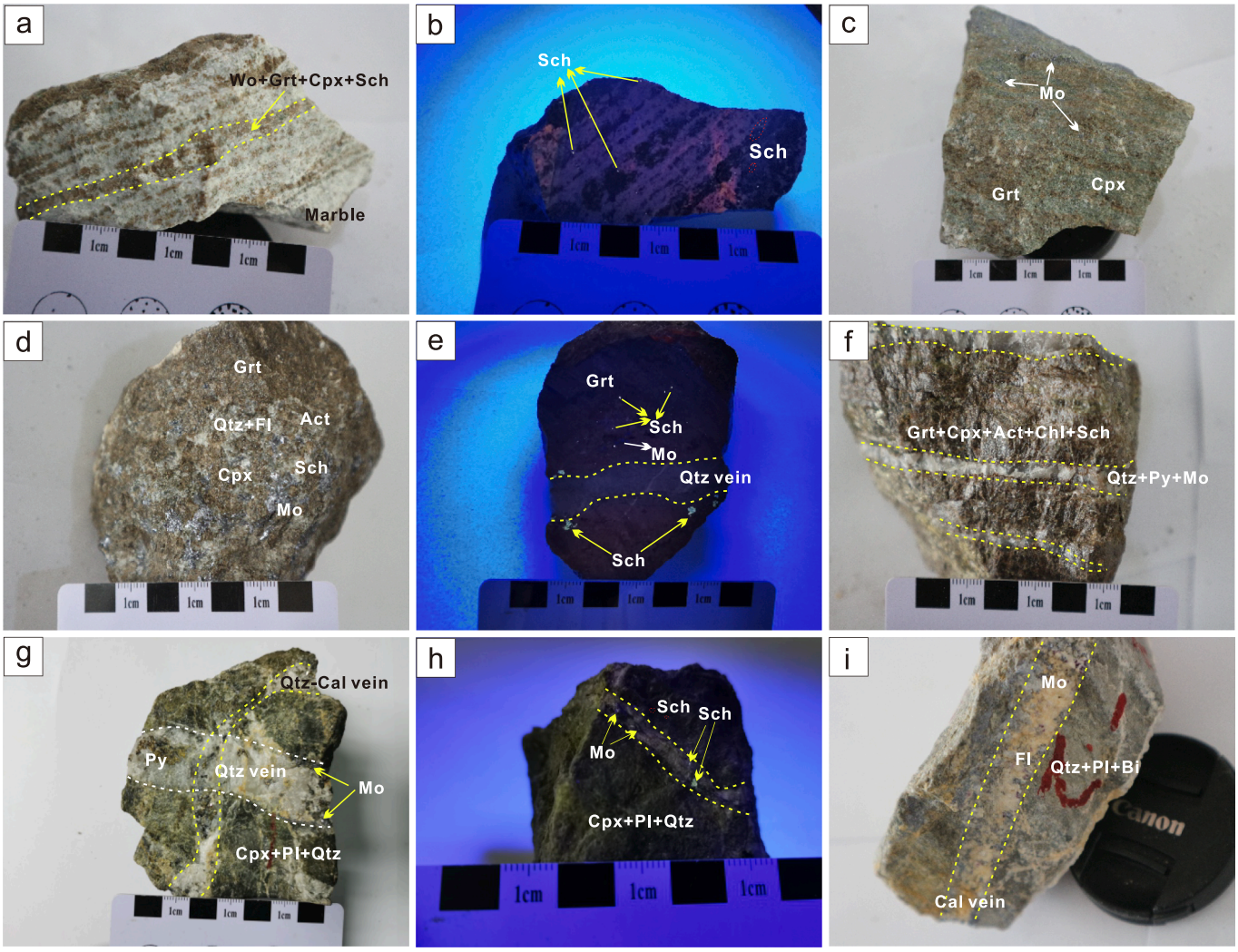

Fig. 5. Photographs of hand specimens in the Sandaozhuang deposit. (a) Hand sample of marble, with garnet-clinopyroxene-wollastonite-scheelite vein crosscutting it. (b) Hand sample of marble under ultraviolet light. Disseminated fine-grained scheelite is distributed in the garnet-clinopyroxene-wollastonite-scheelite veins. (c) Garnet-clinopyroxene skarn of the prograde stage containing disseminated fine-grained molybdenite. (d) Disseminated scheelite and molybdenite mineralization in garnet-actinolite skarn, coexisting with coarse-grained fluorite and quartz. (e) Hand sample of massive garnet-epidote skarn ore under ultraviolet light. Scheelite with fluorescence color and molybdenite are distributed in massive skarn ore. (f) Molybdenite-bearing quartz veins crosscut the garnet-actinolite skarn ore containing disseminated scheelite. (g) Diopside-plagioclase hornfels crosscut by molybdenite-bearing quartz vein, and molybdenite precipitates at the sidewall of the vein. (h) Scheelite occurs in the molybdenite-bearing quartz vein and spreads in massive diopside-plagioclase hornfels ore under ultraviolet light. (i) Hornfels ore crosscut by the molybdenite-bearing calcite vein. Cpx = clinopyroxene, Grt = garnet, Wo = wollastonite, Qtz = quartz, Fl = fluorite, Act = actinolite, Ep = epidote, Sch = scheelite, Mo = molybdenite, Chl = chlorite, Cal = calcite, Py = Pyrite, Pl = plagioclase.

ranging from 2.57 to 24.45% with CaO from 20.74 to 23.56%. Sch A-3 also show high MoO_3 concentrations ranging from 8.25 to12.14% with CaO from 21.51 to 22.03%. On the contrary, Sch B has low MoO_3 concentrations ranging from 0.19 to 1.52% with CaO from 20.10 to 20.90%. Furthermore, Sch C shows low MoO_3 concentrations ranging from 0.20 to 0.97% with CaO from 19.94 to 20.78%. All scheelites have negligible amounts of TiO_2, ZnO, K_2O, Na_2O, FeO, MnO, and PbO.

5.2.2. Trace elements compositions

A total of 84 trace element analyses spots were carried out on 29 scheelite samples from Sandaozhuang (Supplementary Table S1). Sch A-1 shows ΣREE contents ranging from 70 to 120 ppm, Sr contents range from 106 to 126 ppm, and Y/Ho radios range from 20 to 29. Sch A-2 shows ΣREE contents ranging from 168 to 786 ppm, Sr contents range from 14 to 80 ppm, and Y/Ho radios range from 7 to 44. Sch A-3 shows high ΣREE contents ranging from 839 to 1329 ppm, and Sr contents range from 68 to 81 ppm, and Y/Ho radios range from 14 to 20. Sch B shows relatively low ΣREE contents ranging from 59 to 203 ppm, Sr contents range from 28 to 68 ppm, and Y/Ho radios range from 9 to 69. Sch C grains show high ΣREE contents range from 1247 to 5456 ppm, Sr contents range from 64 to 107 ppm, and Y/Ho radios range from 18 to 24.

Chondrite-normalized REE patterns of the three generations of scheelites are shown in Fig. 9. Mo-ΣREE, Mo-δEu and Sr-δEu diagrams are shown in Fig. 10. The Y vs. Ho diagram is shown in Fig. 11. Sch A is characterized by LREE-enriched patterns and negative Eu anomaly (0.35–0.64 in Sch A-1; 0.25–1.07 in Sch A-2; 0.40–0.54 in Sch A-3). Sch A-1 and Sch A-2 have lower ΣREE contents compared with Sch A-3, and is more HREE-depleted. Sch B samples show LREE-enriched and HREE-depleted REE patterns, with HREE contents mainly below the detection limit, and have a positive Eu anomaly (0.75–2.63). Sch C has significantly high ΣREE contents, and chondrite-normalized REE patterns of Sch C show a gradual increase from La to Nd, and a gradual decrease from Nd to Lu, with a remarkable negative Eu anomaly (0.25–0.55).

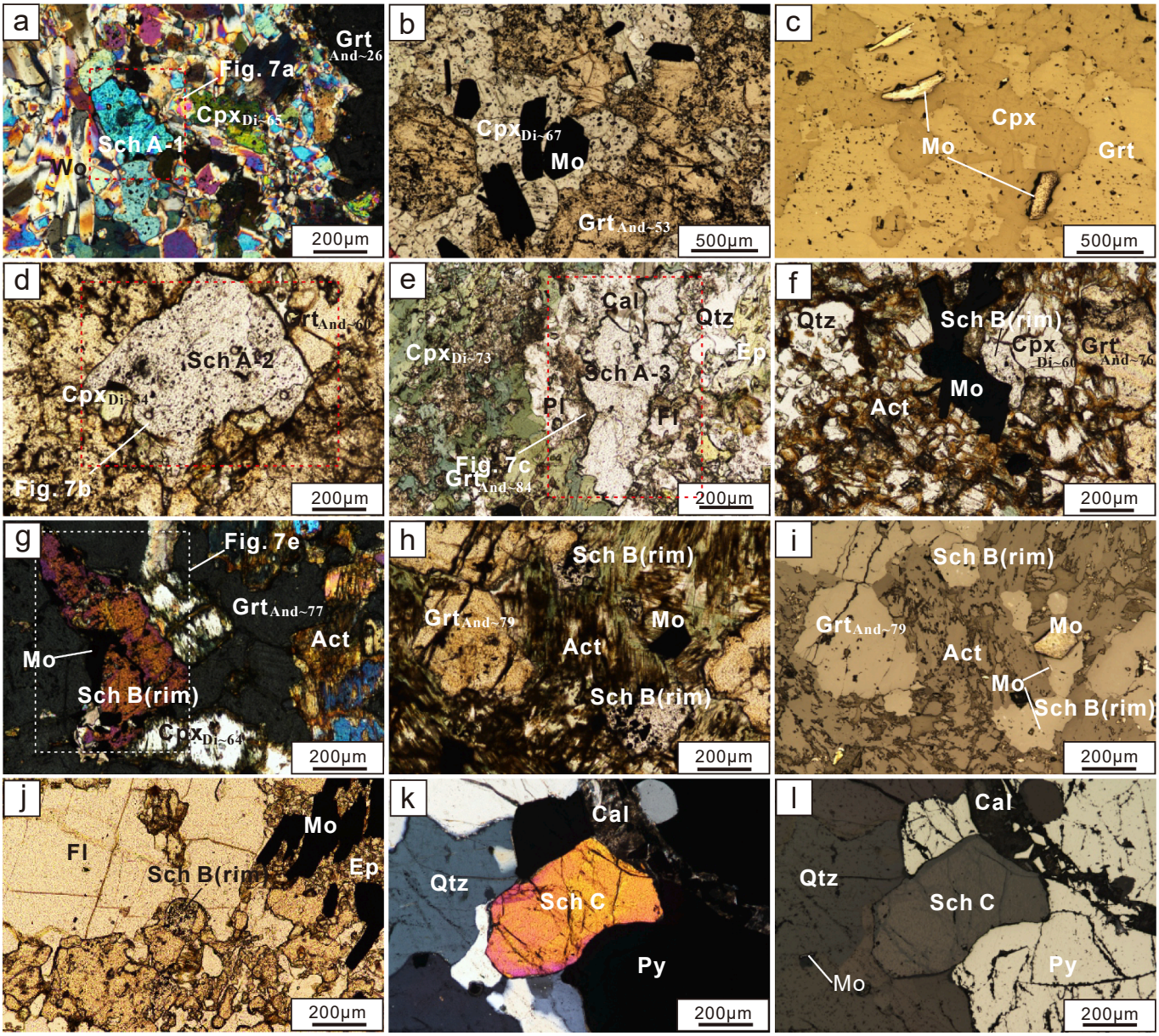

Fig. 6. Microphotographs of mineral assemblages in the Sandaozhuang deposit. (a) Anhedral fine-grained scheelite coexists with diopside, Al-rich garnet and, wollastonite. (b-c) Molybdenite occurring as disseminated grains coexists with diopside and intermediate Fe-rich garnet of the early prograde stage. (d) Early prograde skarn assemblages of scheelite, diopside, and Fe-rich garnet. (e) Scheelite coexists with diopside, plagioclase and quartz in the diopside-plagioclase hornfels. (f-g) Scheelite and molybdenite of the retrograde skarn stage coexist closely and diopside is replaced by actinolite. (h-i) Retrograde skarn assemblages of scheelite, molybdenite and actinolite overprint on the earlier Fe-rich garnet. (j) Fine-grained scheelite of the retrograde skarn stage coexists with fluorite, molybdenite and Fe-rich garnet partly replaced by epidote. (k-l) Euhedral scheelite occurs in pyrite- molybdenite-quartz vein which is cut through by calcite vein. (b, d-f, h, j) were taken under plane transmitted light; (a, g, k) were taken under crossed transmitted light; (c, i, l) were taken under reflected light. Wo = wollastonite, Cpx = clinopyroxene, Sch = scheelite, Grt = garnet, Ep = epidote, Fl = fluorite, Mo = molybdenite, Act = actinolite, Qtz = quartz, Cal = calcite, Py = Pyrite, Pl = plagioclase.

5.2.3. *Trace element mapping of scheelite*

A representative individual scheelite grain in the retrograde stage was selected for LA-ICP-MS trace element mapping to further explore the relationship between CL image features and distribution of trace elements. Sample 18SDZ-40–1 M consists of a CL-dark Sch A-2 rimmed by CL-bright Sch B (Fig. 12a). Sch A-2 shows higher levels of Mn, Mo, Nb, U, and LREE, and lower levels of Eu and Gd compared with Sch B. Notably, Mo contents in the early generation Sch A-2 to the late generation Sch B decrease significantly (Fig. 12f). Both Sch A-2 and Sch B are depleted in HREE, and it is difficult to detect the signal value of HREE from Er. In addition, Sch A-2 and Sch B have similarly low Sr and Na contents.

5.3. *Major and trace elements composition of garnet and clinoproxene*

Major element results of garnet and clinoproxene are listed in Supplementary Table S2, and graphically presented in Fig. 13. Most garnets in the prograde stage at Sandaozhuang deposit are Fe-rich andradite, with high concentrations of FeO (15.71–27.08%), coexisting with the high-Mo Sch A-2 (Fig. 6d). While we also found that a few Al-rich grossular with a small amount of FeO (6.87–8.96%) coexist with relatively low-Mo Sch A-1 in the early prograde stage (Fig. 6a). All garnets with very low concentrations of MnO (0.02–2.67%) are classified as almandine-grossularite varieties (Fig. 13a). Clinoproxene from the Sandaozhuang deposit is mainly Mg-rich diopside with minor johannsenite (MnO) component and hedenbergite (FeO) component (Fig. 13b).

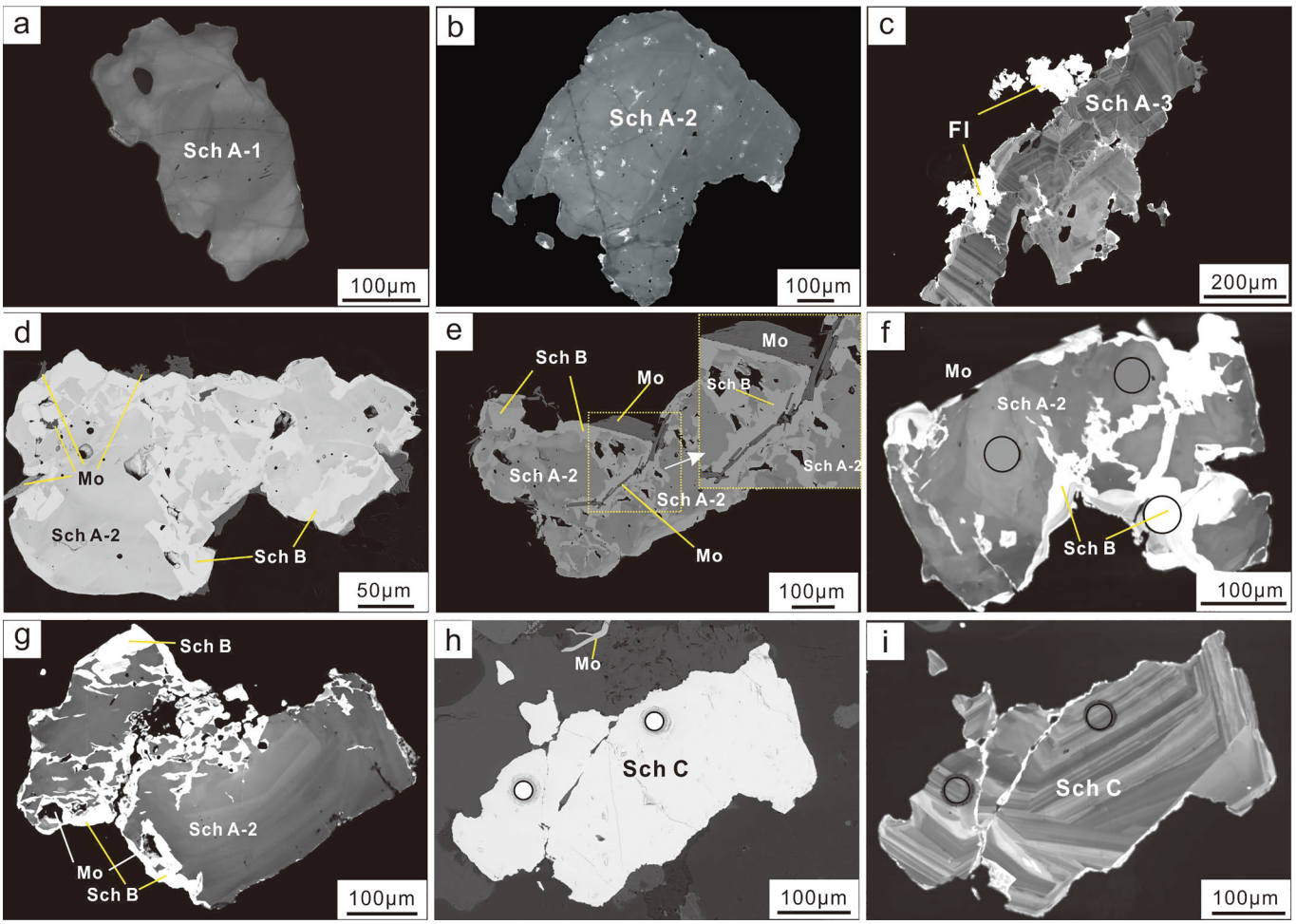

Fig. 7. Cathodoluminescence (CL) images (a-c, f-g, i) and back-scattered electron (BSE) images (d-e, h) of scheelite.

Table 1
Summary of Electron Microprobe Analyses of scheelite from the Sandaozhuang W-Mo Skarn Deposit (values in wt%).

Type		MoO_3	TiO_2	ZnO	Na_2O	K_2O	FeO	MnO	WO_3	CaO	PbO	Total
Sch A-1	Min	1.57	0.00	0.00	0.00	0.00	0.00	0.00	75.23	20.40	0.00	97.78
n = 8	Average	1.90	0.00	0.00	0.02	0.00	0.00	0.00	77.04	20.67	0.00	99.64
	Max	2.23	0.01	0.02	0.05	0.01	0.01	0.01	77.85	20.91	0.00	100.76
	sd	0.17	0.00	0.01	0.02	0.00	0.00	0.01	0.78	0.18	0.00	0.82
	Median	1.87	0.00	0.00	0.01	0.00	0.00	0.00	77.24	20.69	0.00	99.82
Sch A-2	Min	2.57	0.00	0.00	0.00	0.00	0.00	0.00	51.79	20.74	0.00	96.64
n = 35	Average	12.01	0.00	0.01	0.01	0.00	0.02	0.01	65.57	22.03	0.00	99.68
	Max	24.45	0.03	0.06	0.03	0.02	0.21	0.04	77.41	23.56	0.03	102.38
	sd	5.96	0.01	0.02	0.01	0.01	0.04	0.01	6.74	0.75	0.01	1.08
	Median	12.90	0.00	0.00	0.01	0.00	0.01	0.00	65.24	22.02	0.00	99.70
Sch A-3	Min	8.25	0.00	0.00	0.00	0.00	0.00	0.00	65.18	21.51	0.00	98.69
n = 5	Average	9.61	0.00	0.03	0.02	0.00	0.00	0.00	68.59	21.71	0.00	99.96
	Max	12.14	0.00	0.07	0.05	0.00	0.00	0.02	70.26	22.03	0.00	101.22
	sd	1.35	0.00	0.03	0.02	0.00	0.00	0.01	1.89	0.20	0.00	0.85
	Median	9.25	0.00	0.01	0.00	0.00	0.00	0.00	69.67	21.63	0.00	100.17
Sch B	Min	0.19	0.00	0.00	0.00	0.00	0.00	0.00	76.60	20.10	0.00	98.28
n = 19	Average	0.74	0.00	0.01	0.01	0.01	0.03	0.01	78.39	20.60	0.01	99.81
	Max	1.52	0.00	0.06	0.06	0.02	0.24	0.02	80.81	20.90	0.09	101.86
	sd	0.39	0.00	0.02	0.02	0.01	0.05	0.01	1.10	0.20	0.02	1.08
	Median	0.85	0.00	0.00	0.01	0.00	0.02	0.01	78.14	20.64	0.00	99.68
Sch C	Min	0.20	0.00	0.00	0.01	0.00	0.00	0.00	76.70	19.94	0.00	97.59
n = 10	Average	0.44	0.00	0.01	0.04	0.00	0.05	0.00	78.33	20.47	0.02	99.37
	Max	0.97	0.00	0.05	0.08	0.02	0.21	0.01	79.79	20.78	0.13	100.47
	sd	0.25	0.00	0.02	0.02	0.01	0.08	0.01	0.95	0.28	0.04	0.91
	Median	0.34	0.00	0.00	0.03	0.00	0.01	0.00	78.39	20.51	0.00	99.54

Note: sd = standard deviation.

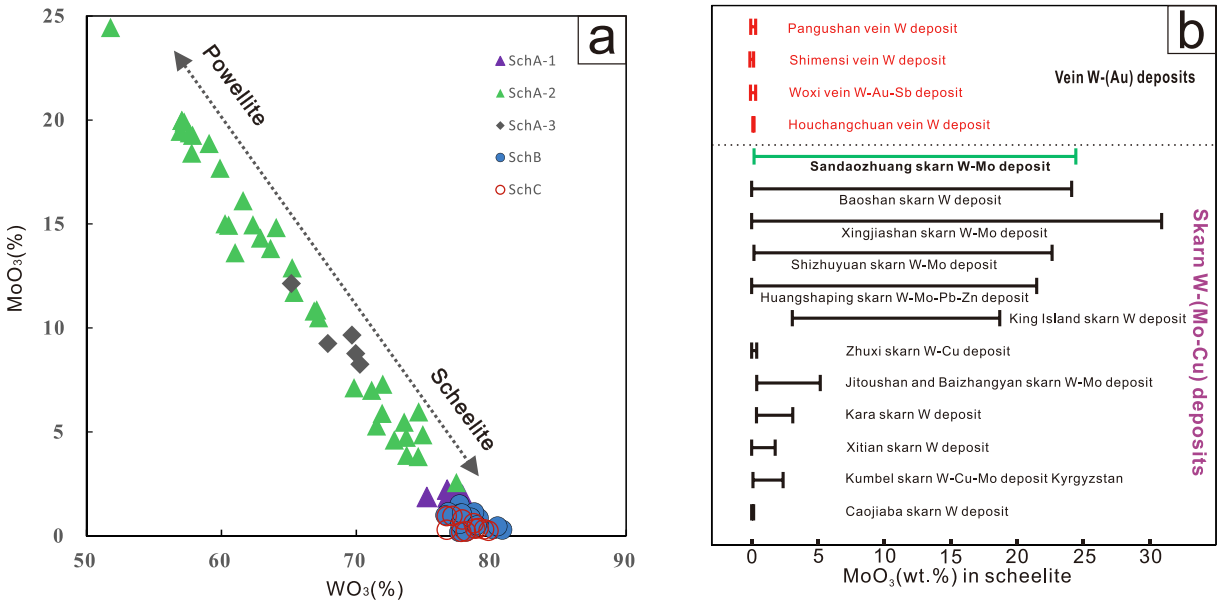

Fig. 8. (a) Plot of MoO_3 vs. WO_3 of scheelites from the Sandaozhuang deposit; (b) Comparison of MoO_3contents (%) in scheelite between the Sandaozhuang deposit with and different types of tungsten deposits in the world, with data from (Kwak and Tan, 1981; Sun and Ren, 1986; Zaw and Singoyi, 2000; Peng et al., 2003; Wang et al., 2010; Yu, 2012; Song et al., 2014; Soloviev, 2015; Sun and Chen, 2017; Xie et al., 2019; Ding et al., 2018; Zhao et al., 2018; Liu et al., 2019; Sun et al., 2019; Liu et al., 2020).

Trace element results of garnet and clinoproxene are presented in Supplementary Table S3. Clinoproxenes from Sandaozhuang have negligible REE contents, however, the REE + Y contents of garnet range from 36.98 to 233.25 ppm, the REE patterns of garnet are shown in Fig. 9d.

5.4. Sr-Nd isotope compositions of scheelite

Sr and Nd isotope data for eight scheelite samples from the Sandaozhuang deposit are presented in Table 2. Analysis show variation in Sm (1.31–6.37 ppm), Nd (18.2–71.9 ppm), with $^{147}Sm/^{144}Nd$ = 0.0328–0.0574 and $^{143}Nd/^{144}Nd$ = 0.511731–0.511882, and the $\varepsilon_{Nd}(t)$ values range from − 14.7 to − 11.9. Initial $^{87}Sr/^{86}Sr$ values of these scheelites range from 0.7158 to 0.7295.

6. Discussion

6.1. Mechanisms controlling REE patterns in scheelite

REE patterns of scheelite have been widely applied to infer signatures and evolution of ore-forming fluid (Zhao et al., 2018; Li et al., 2018; Liu et al., 2020). Findings on mineral assemblages, CL and BSE characteristics, and elemental maps, show that Sch A is the earliest precipitated scheelites, with Sch B forming later, and Sch C formed in the last stage. Scheelite in different stages from early to late generation exhibits various REE patterns. REE patterns of scheelite are affected by several factors and the main factor is different REE substitution mechanisms caused by scheelite crystal chemistry.

Different substitution mechanisms that introduce REEs into the scheelite result in different REE patterns in scheelite (Ghaderi et al. 1999). Three substitution mechanisms have been proposed by Nassau and Loiacono (1963), Burt (1989) and Ghaderi et al. (1999): (M1) $2Ca^{2+} = REE^{3+} + Na^{+}$; (M2) $Ca^{2+} + W^{6+} = REE^{3+} + Nb^{5+}$; (M3) $3Ca^{2+} = 2REE^{3+} + \square Ca$, where □Ca represents a Ca-site vacancy. The M1 and M2 mechanisms require coupling substitution with charge balance compensation, and the degree of this substitution depends on Na and Nb contents in scheelite (Ghaderi et al., 1999). Moreover, the M1 and M2 substitution mechanisms result in MREEs-enriched patterns of scheelites based on the theoretical calculation (Ghaderi et al., 1999; Sun et al., 2019).

In the Sandaozhuang deposit, Sch A and Sch B related to skarn mineralization do not show the humped patterns (MREEs-enriched). In addition, they have very low contents of Na_2O and Nb, and the lack of correlation between Na/Nb and REE + Y-Eu (atom; Fig. 14) suggests that M1 and M2 substitutions are not the principle mechanism in these scheelites. The REE patterns of the Sch A and Sch B are best explained by the M3 substitution mechanism, in which REE ions are substituted in pairs into scheelite structure with a vacant Ca site. The relatively high concentrations of Na_2O and positive correlation between Na atoms and REE + Y–Eu atoms (Fig. 14a) indicate that the M1 mechanism is involved in the formation of Sch C grains from the quartz-sulfide vein. The M1 substitution can lead to remarkable MREE fractionation, because the MREE with ionic radius close to 1.06 Å would preferentially enter the lattice by substitution in the Ca site (Ghaderi et al., 1999; Brugger et al., 2002) ($^{[8]}rCa^{2+}$= 1.12 Å; $^{[8]}rEu^{3+}$= 1.06 Å; Shannon, 1976). Therefore, the convex LREE pattern of Sch C with LREE (Ce-Sm) fractionation from the quartz-sulfide vein is mainly attributed to the strong crystallographic control on the incorporation of MREE by the M1 substitution.

In addition to the crystal chemistry, variation in REE patterns of scheelite may be affected by redox condition, pH, pressure, fluid composition and crystallization of REE-enriched minerals (Song et al., 2014; Su et al., 2019; Liu et al., 2020). However, the redox environment, pH, and pressure can only change the partition coefficient of some individual rare earth elements, and cannot result in the whole fractionation of REE in scheelite (Green and Pearson, 1983; Wood and Samson, 2000; Brugger et al., 2008; Liu et al., 2020). Results on $\delta^{13}C$-$\delta^{18}O$-δD values reported by Xiang et al (2012b) indicate that the ore-forming fluids were mainly derived from a single hydrothermal system and there may be lack of meteoric fluid mixing. Therefore, crystallization of REE-enriched minerals may play a key role in fractionation of REE in the evolved ore-forming fluid.

The Sch A-1, Sch A-2 and Sch B from the skarn ores show a typical right-dip-type REE_N pattern, enriched in LREE and strongly depleted in HREE with a negative to positive Eu anomaly (Fig. 9). The Sch B is more depleted in HREEs, and has lower REE contents compared with Sch A.

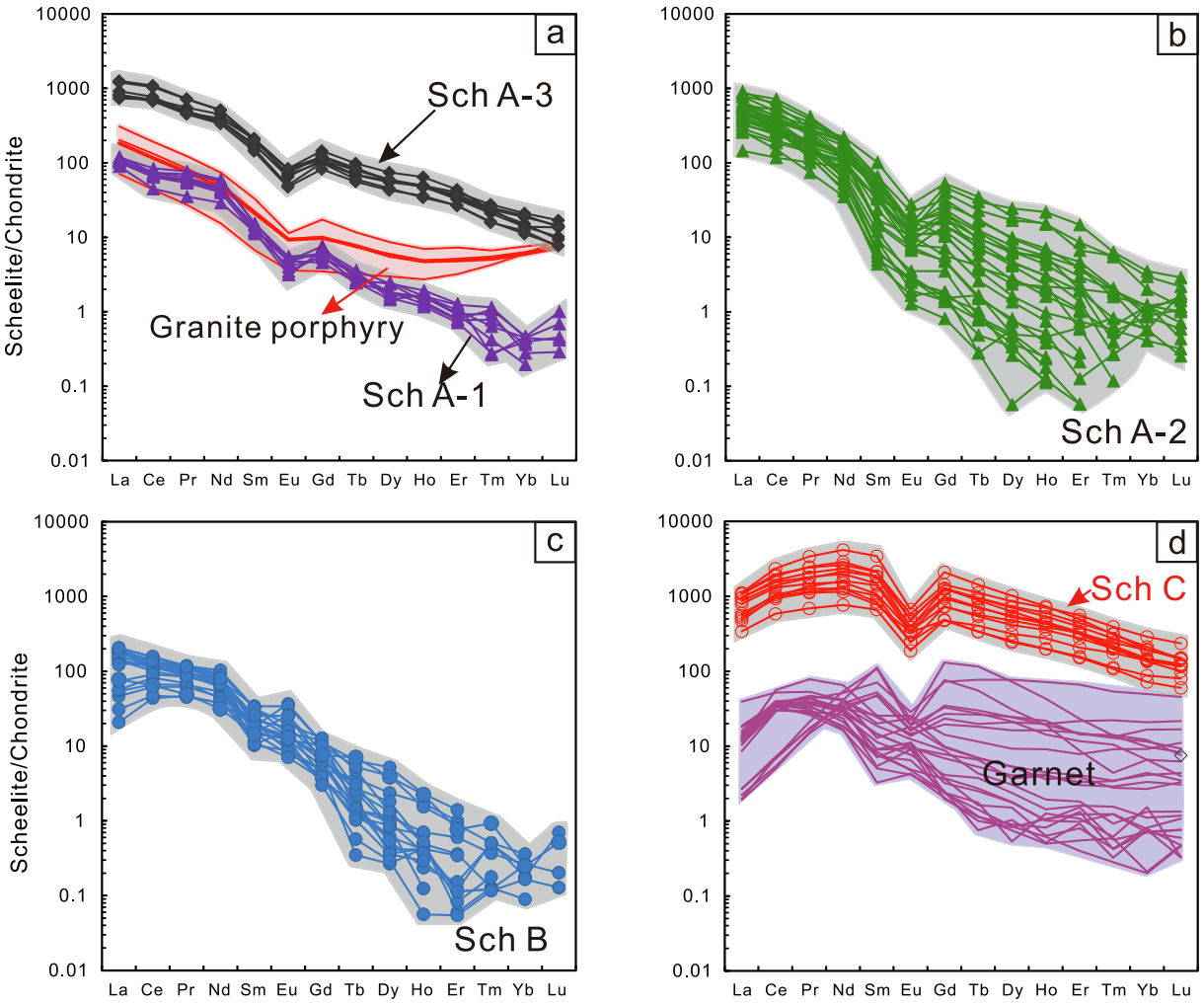

Fig. 9. Chondrite-normalized REE patterns of scheelites and garnets from the Sandaozhuang deposit. The REE patterns of Nannihu granite from Sandaozhuang are also exhibited for comparison. The normalization values were taken from McDonough and Sun (1995). The granite data are collected from Bao et al. (2014).

Mapping results can also directly reflect that the content of LREE from Sch A-2 to Sch B is significantly reduced, and their HREE are depleted (Fig. 12). Later generation Sch B may replace Sch A-2 through a dissolution and reprecipitation process, and compositional exchange between early generation Sch A-2 and fluid of retrograde skarn stage may result in different REE patterns, Eu anomalies and Mo content in Sch B compared with Sch A-2. Since no other external fluid is added to the hydrothermal system, changes in compositions of the fluid may be caused by the mineral assemblage in skarn ores (garnet + diopside + scheelite + epidote), and the garnet and diopside can accommodate REE^{3+} by substituting divalent cation (Fe, Mn, Mg or Ca^{2+}) (Enami et al., 1995; Jaffe, 1951; Van Orman et al., 2001). Therefore, precipitation of these REE-enriched skarn minerals may cause a significant decrease in total REE and depletion of HREE in residual fluids of the retrograde skarn stage. The Sch A-2 can react with such a fluid and dissolve to form Sch B.

A large amount of garnet and diopside precipitated in prograde skarn stage, and crystallized prior to Sch B, and Sch A-1 and Sch A-2 may also be influenced by these skarn minerals. In view of these, we mainly analyzed the trace elements of garnet and diopside in the Sandaozhuang deposit. The results show that diopside has negligible REE content, however, REE + Y contents in garnet range from 37.0 to 233 ppm and HREE/LREE ratios range from 1.84 to 295.41 (Supplementary Table S3), indicating that strong HREE enrichment occurred in garnets.

The Sch A-3 grains disseminated in the diopside-plagioclase hornfels are characteristic by high REE contents and no remarkable depletion of HREEs. The Sch C precipitated in the latest stage quartz-sulfide veins shows a high REE content and a slightly right dipping REE pattern. These quartz veins containing a small amount of scheelite mainly occur in pyroxene skarn and diopside-plagioclase hornfels. Sch A-3 and Sch C have high REE contents, and their HREEs are not so depleted which is mainly due to the lack of garnet and the low REE content in diopside.

As discussed above, the REE patterns of Sch A and Sch B can be best explained by the $3Ca^{2+} = 2REE^{3+} + \square Ca$ substitution, in which the REE ions enter the scheelite structure in pairs, which is related to a Ca-site vacancy. According to Coulomb's minimum energy law, the Ca-site vacancy is located between two REE-substitution sites. There is such a vacancy, which makes them flexible to contain REEs of any size (Ghaderi et al., 1999). Therefore, the primary Sch A can inherit the LREE-enriched characteristics and negative Eu anomaly of the initial ore-forming fluid derived from the Nannihu granite porphyry. The depletion of HREE might result from the precipitation of REE-enriched minerals (e.g., garnet) during the evolution of ore-forming fluids.

6.2. *The origin of ore-forming fluids and materials*

The element pair Y-Ho exhibit similar geochemical behavior due to the similar ionic radii and valence (Bau and Dulski, 1995). Therefore, Y/Ho ratios are fairly stable in clastic sediments and igneous rocks (Bau, 1996). However, Y/Ho ratios in hydrothermal deposits are affected by fluid mixing and chemical complexation (Su et al., 2019; Liu et al., 2020). In Sandaozhuang, Y/Ho ratios of scheelite are relatively uniform

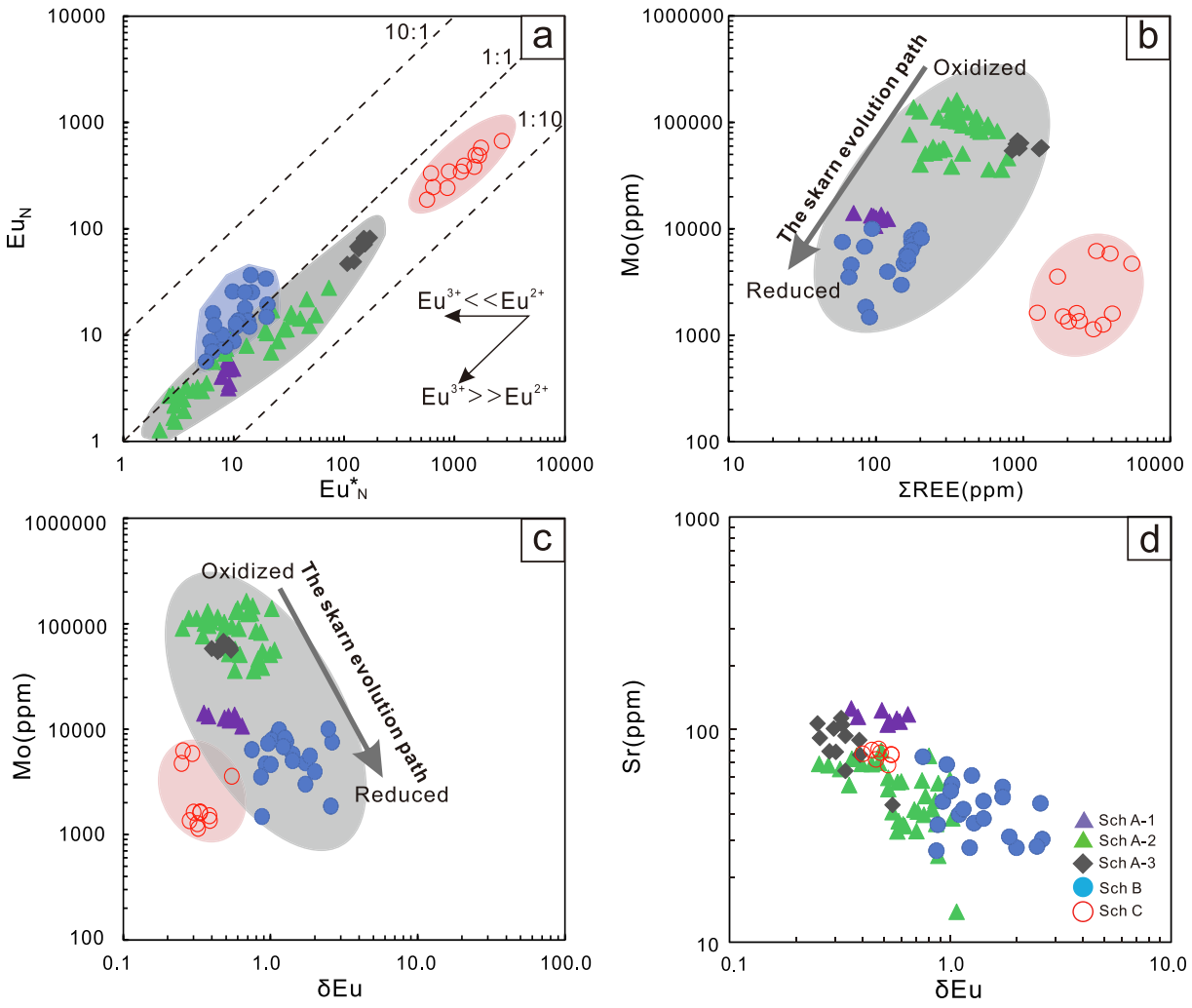

Fig. 10. (a) Plot of chondrite-normalized Eu concentrations (Eu_N) versus calculated Eu^*_N values for scheelites, where $Eu^*_N = (Sm_N \times Gd_N)^{1/2}$. (b) Plot of Mo versus total REEs (ΣREE) of scheelites; (c) Plot of δEu versus Mo of scheelites; (d) Plot of δEu versus Sr of scheelites.

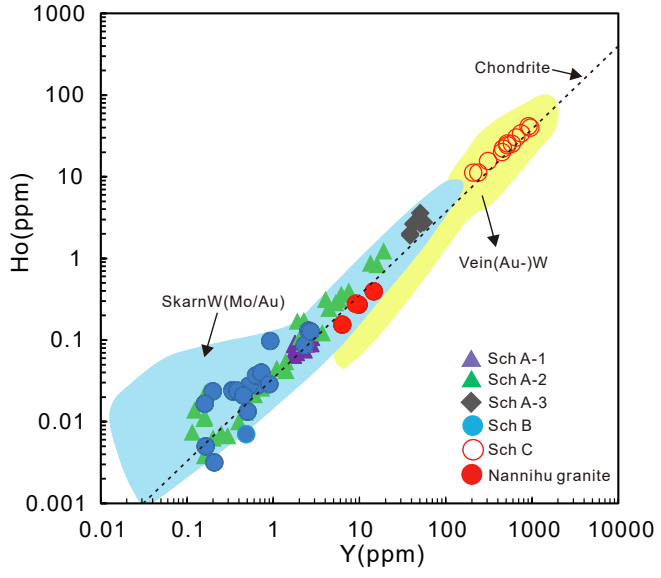

Fig. 11. The Y vs. Ho for scheelites from the Sandaozhuang deposit. The granite data are collected from Bao et al. (2014). The chondrite line is from Bau (1996). The skarn W (Mo/Au) and vein (Au-) W field are from Li et al. (2019).

and consistent with the Nannihu granite porphyry (Fig. 11), suggesting that ore-forming fluids responsible for scheelites are mainly derived from the Nannihu granite porphyry. This finding is consistent with reports from C- O–H isotopic studies, which report that the ore-forming fluids of the Sandaozhuang deposit are dominantly derived from a magmatic source (Xiang et al., 2012b).

Sr and Nd isotopic signatures of scheelite in the hydrothermal deposit are widely applied to trace the source of ore-forming fluids and record the fluid-rock interaction (Bell et al., 1989; Brugger et al., 2002; Song et al., 2014; Sun and Chen, 2017; Sun et al., 2019; Song et al., 2019; Han et al., 2020). Scheelite is characterized by high and stable Sm/Nd ratios, therefore, Sm-Nd isotope system is useful for Sm/Nd dating and Nd isotopic studies in ore deposit (Kent et al., 1995; Voicu et al., 2000; Sun et al., 2019). Scheelite lattice can accommodate Sr but rejects Rb, resulting in very low Rb/Sr ratios in scheelite (Deer et al., 1966). At Sandaozhuang, the content of Sr in scheelite ranges from 30.1 to 54.2 ppm, but the content of Rb is lower than the detection limit. Thus the measured Sr isotope ratio can directly reflect Sr isotope composition of the ore-forming fluid during scheelite crystallization (Bell et al., 1989; Han et al., 2020).

Scheelites in the tungsten deposits have low $\varepsilon_{Nd}(t)$ (mostly < -7) and high ($^{87}Sr/^{86}Sr)_i$ (mostly greater than 0.710) (Song et al., 2014; Sun and Chen, 2017; Sun et al., 2019), which are different from the scheelite in vein-type gold deposits dominated by mantle materials (Fig. 15a). Scheelite samples from Sandaozhuang show a narrow and low range of

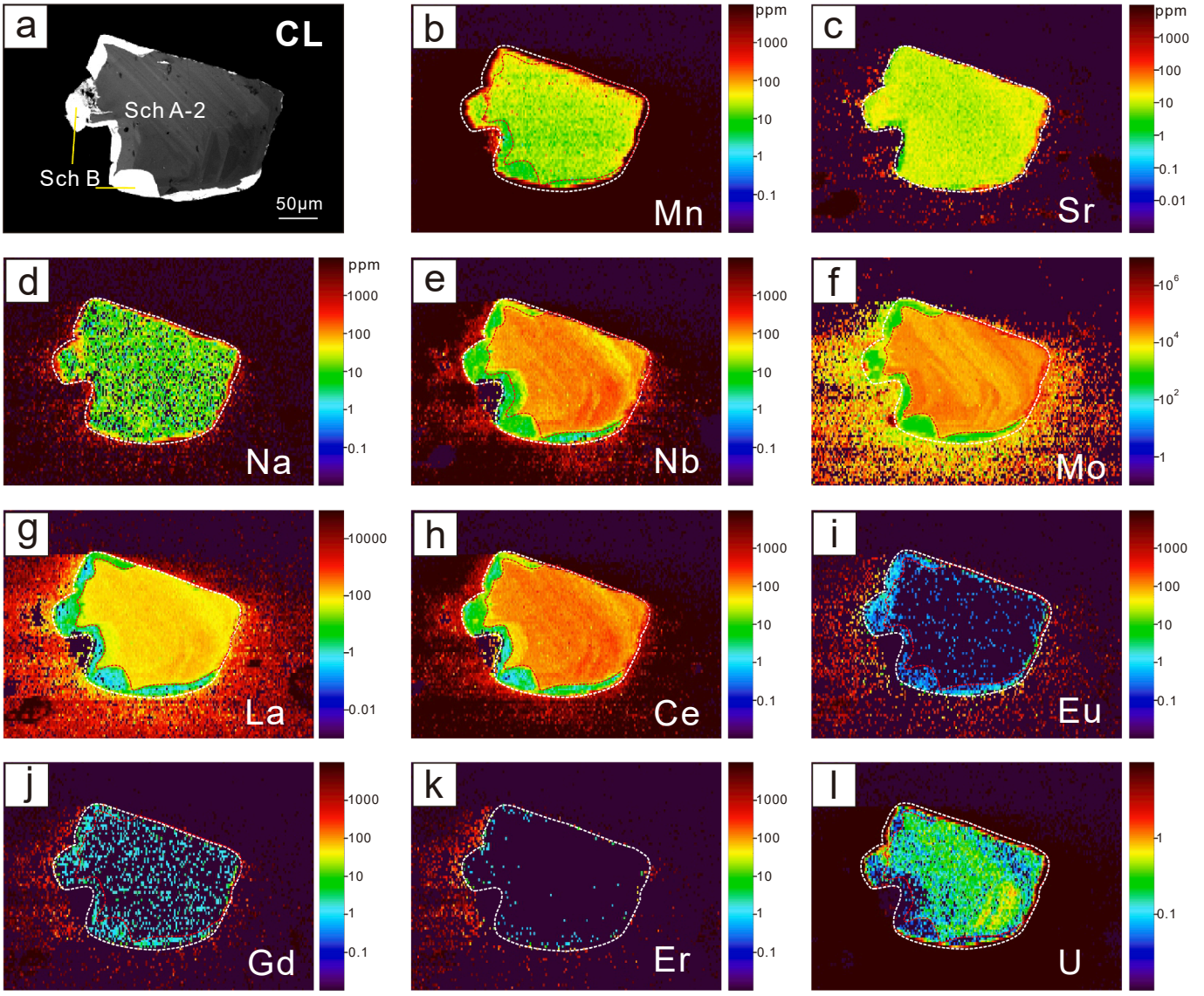

Fig. 12. Cathodoluminescence (CL) images and LA-ICP-MS trace element mapping of scheelite (sample 18SDZ-40–1 M). Scale in part per million (ppm).

$\varepsilon_{Nd}(t)$ values from − 14.7 to − 11.8 (Fig. 15a; Table 2). The $\varepsilon_{Nd}(t)$ values of scheelite are basically consistent with that of the Nannihu granite porphyry (−17.5 ~ − 11.3; Bao et al., 2014), suggesting that granitic magmas are a significant origin for the mineralizing fluids. However, scheelite samples from Sandaozhuang deposit show high $(^{87}Sr/^{86}Sr)_i$ values from 0.7158 to 0.7295 (average value = 0.7204), which are significantly higher compared with the values for the Nannihu granite porphyry (0.7069 ~ 0.7080; Fig. 15) and other granites from the Luanchuan Mo field with Sr isotopic ratios ranging from 0.7047 to 0.7098 (Chen et al., 2000). Therefore, the high Sr isotopic composition of scheelites in Sandaozhuang needs an additional radiogenic ^{87}Sr source. The Meso-Neoproterozoic Guandaokou Group and Luanchuan Group low-grade *meta*-sedimentary rocks in this area have a high and wide $(^{87}Sr/^{86}Sr)_i$ ratios from 0.7153 to 0.8328 (average value = 0.7610; Fig. 15b), which may be the source of Sr isotopes. Interaction between ore-forming fluids derived from the granite porphyry and Luanchuan Group country rocks may introduce additional radiogenic ^{87}Sr and significantly increase Sr isotopic ratios of the fluids. The Nd isotopic data of the Luanchuan Group are not available. However, the REE content in the carbonate rocks is very low (Supplementary Table S4), so that the skarnization could introduce significant Sr but very limited REEs (including Nd) into the ore-forming fluids. It is thus inferred that the reaction between hydrothermal fluid derived from the magma and surrounding rock may not significantly change the Nd isotope composition of scheelite.

Tungsten mineralization in Sandaozhuang is closely related to the Nannihu granite porphyry, from which tungsten metals were exsoluted along with the initial ore-forming fluids. A small fraction of tungsten may be leached into the metallogenic fluid through the fluid-rock interaction as discussed above, due to the high tungsten contents in the Luanchuan Group *meta*-sedimentary country rocks (1.82–9.81 ppm; Xiao and Sun, 2007). However, the tungsten in strata is not high enough to form such a super-large tungsten deposit, and most tungsten is likely to be originated from the magma. The intense fluid-rock interaction also resulted in the formation of Ca^{2+}-rich hydrothermal fluids, and significantly promoted the precipitation of scheelite. Analysis of the trace elements in the marble without metasomatism of Sanchuan Formation in the Sandaozhuang mining area, show that the tungsten content (average 0.60 ppm) is very low (Supplementary Table S4), therefore it is difficult to be a tungsten source.

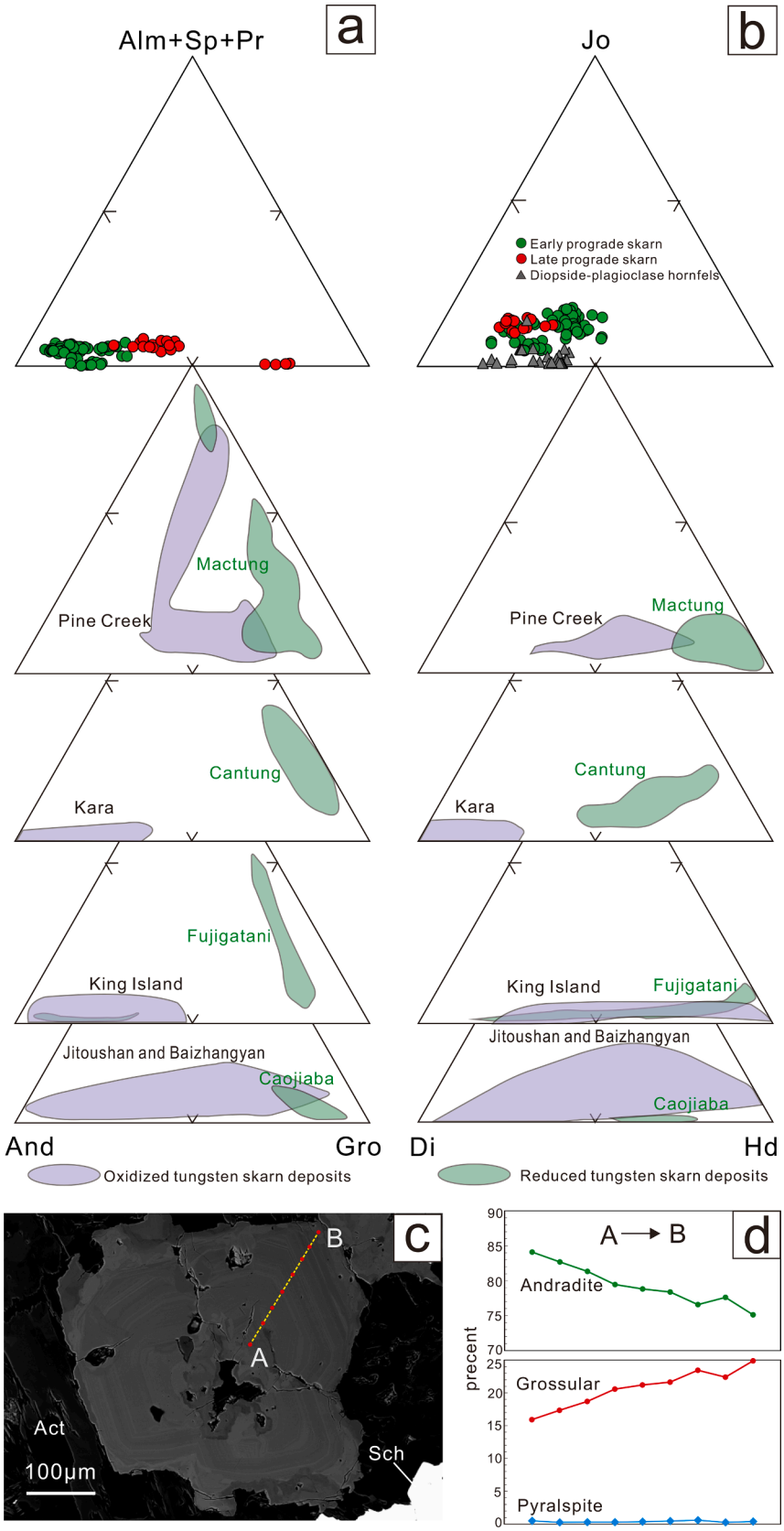

Fig. 13. Ternary diagrams showing compositional variation of garnet (a), expressed in relative portions of andradite (And), grossular (Gro) and Almandine + Spessartine + Pyrope (Alm + Sp + Pr) end-members, and clinopyroxene (b), expressed in relative portions of diopside (Di), hedenbergite (Hd) and johannsonite (Jo) end-members from the Sandaozhuang tungsten skarn deposit compared with garnet and clinopyroxene from oxidized tungsten deposits at Baizhangyan, Kara, King Island, Jitoushan, and Pine Creek (Zaw and Singoyi, 2000; Newberry, 1982; Kwak and Tan, 1981; Song, 2010) and reduced tungsten skarn deposits at Cantung, Caojiaba, Fujigatani, and Mactung (Einaudi et al., 1981; Zaw and Singoyi, 2000; Sato, 1980; Xie et al., 2019). (c) BSE image of a subhedral garnet grain of the late prograde stage from Sandaozhuang. (d) Core–rim profile of garnet from Sandaozhuang showing variations in andradite, grossular, and pyralspite compositions. The A–B profile line is shown in Fig. 13c.

Table 2
Results of scheelite Sr-Nd isotopic analysis from the Sandaozhuang W-Mo Deposit.

Sample no.	Age (Ma)	Sm (ppm)	Nd (ppm)	$^{147}Sm/^{144}Nd$	$^{143}Nd/^{144}Nd$	2 σ	$^{143}Nd/^{144}Nd(t)$	εNd (t)	$f_{Sm/Nd}$	$^{87}Sr/^{86}Sr$	2 σ
SDZ-2	150	1.31	18.2	0.0435	0.511882	0.000002	0.511839	−11.8	−0.78	0.716145	0.000009
SDZ-4	150	1.29	23.8	0.0328	0.511785	0.000004	0.511753	−13.5	−0.83	0.721725	0.000008
SDZ-8	150	2.22	34.3	0.0391	0.511767	0.000003	0.511729	−14.0	−0.80	0.715762	0.000005
SDZ-17	150	2.48	26.1	0.0574	0.511846	0.000005	0.511790	−12.8	−0.71	0.729485	0.000009
SDZ-18	150	1.32	20.2	0.0395	0.511797	0.000003	0.511758	−13.4	−0.80	0.718039	0.000006
SDZ-29	150	3.81	45.3	0.0508	0.51174	0.000002	0.511690	−14.7	−0.74	0.720212	0.000009
SDZ-30	150	6.37	71.9	0.0535	0.511749	0.000002	0.511696	−14.6	−0.73	0.721649	0.000008
SDZ-38	150	3.51	61.2	0.0347	0.511731	0.000003	0.511697	−14.6	−0.82	0.719966	0.000004

Note: the mineralization age 150 Ma is from Bao, (2014)

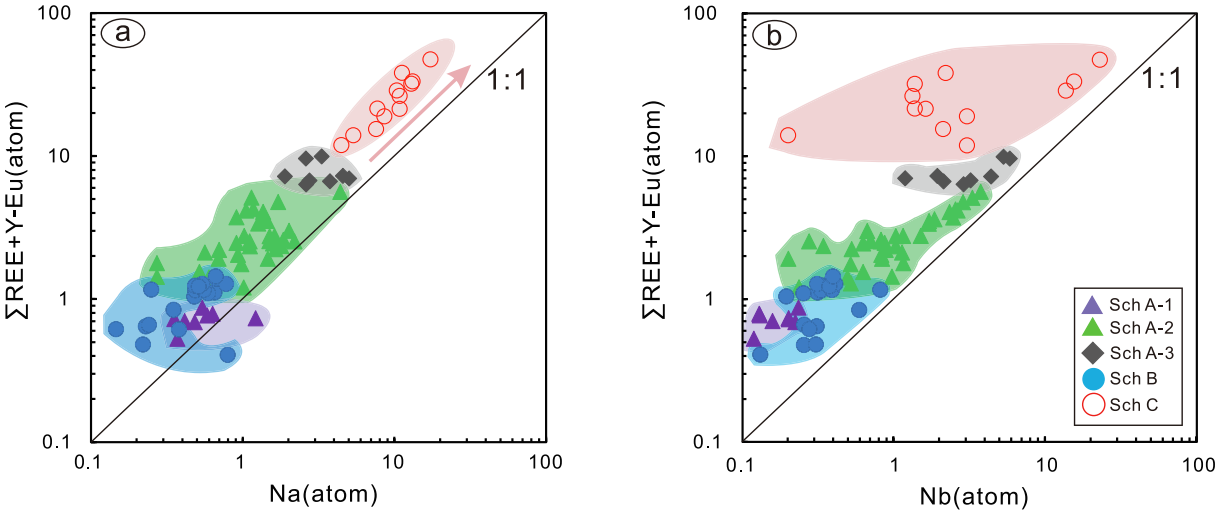

Fig. 14. (a) Plot of Na (atom) versus ΣREE + Y–Eu (atom) for scheelite. (b) Plot of Nb (atom) versus ΣREE + Y–Eu (atom) for scheelite. (Diagram modified from Ghaderi et al., 1999).

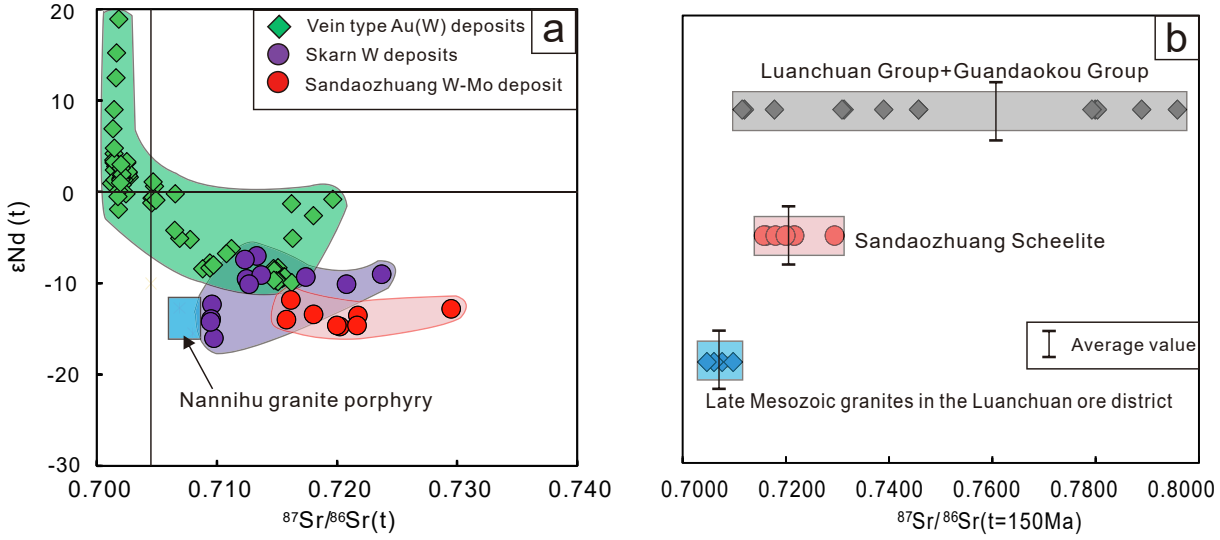

Fig. 15. (a) $(^{87}Sr/^{86}Sr)i$ versus $\varepsilon_{Nd}(t)$ (t = 150 Ma) correlation diagram for scheelites of the Sandaozhuang deposit. The Sr and Nd isotopic data of the Nannihu granite is from Chen et al. (2000) and Bao et al. (2014). The Sr-Nd isotope data of scheelite from vein-type Au (W) deposits were taken from Bell et al. (1989), Kent et al. (1995), Darbyshire et al. (1996), Voicu et al. (2000), Kempe et al. (2001), Brugger et al. (2002), Xiong et al. (2006); the data from skarn W deposits were taken from Song et al. (2014) and Sun et al. (2019). (b) Plot of $^{87}Sr/^{86}Sr$ (t = 150 Ma) ratios for scheelite from the Sandaozhaung deposit. The $^{87}Sr/^{86}Sr$ ratios for Late Mesozoic granites in the Luanchuan ore district are from Chen et al. (2000). The $^{87}Sr/^{86}Sr$ (t = 150 Ma) ratios for Guandaokou group and Luanchuan group rocks are from Qi et al. (2009).

6.3. Redox condition of the ore-forming fluids

6.3.1. Redox condition indicated by Eu valence state

Eu is a redox sensitive element and has two ionic valences: Eu^{3+} and Eu^{2+} (Shannon, 1976). Eu^{3+} can substitute for the major component Ca in scheelite just like other REE^{3+} (Ghaderi et al., 1999). Eu^{3+} has a more similar ionic radius to Ca^{2+} compared with Eu^{2+}, with eight-fold coordination in scheelite ($^{[8]}rEu^{3+}$ = 1.06 Å versus $^{[8]}rEu^{2+}$ = 1.25 Å; $^{[8]}rCa^{2+}$ = 1.12 Å; Shannon, 1976), whereas Eu^{2+} can also substitute for Ca through the M3 mechanism described above (Blundy and Wood, 1994; Liu et al., 2019). Because Eu^{2+} and Ca^{2+} have the same charge, Eu^{2+} is preferentially more incorporated compared with Eu^{3+} (Ghaderi et al., 1999; Song et al., 2014; Yuan et al., 2019).

Valence state of Eu in scheelite can be determined by analyzing correlation among Eu, Sm and Gd (Ghaderi et al., 1999). In Eu^{3+}-dominated fluids, measured Eu_N in scheelite will display a positive relationship with the Eu^*_N where $Eu^*_N = (Sm_N \times Gd_N)^{1/2}$, and it will not significantly affect Eu anomaly, because the behavior of Eu^{3+} is similar to that of Sm^{3+} and Gd^{3+}. On the other hand, Eu_N in scheelite is not correlated with Eu^*_N in scheelite from Eu^{2+}-dominated fluids. In this study, Eu_N in Sch A hosted during the prograde skarn stage consistently change with Eu^*_N, showing a zoned distribution along the 1:1 correlation line (Fig. 10a) and Eu anomalies (δEu) are negative. This finding implies that Eu in the fluid occurs mainly as Eu^{3+} in a relatively oxidized environment, consistent with dominance of negative Eu anomalies. Sch B precipitated in the retrograde skarn stage, however, it diverge from the 1:1 ratio line with high Eu_N/Eu^*_N (Fig. 10a). This observation implies that Eu^{2+} was primarily concentrated in the fluid, which is consistent with dominance of positive Eu anomalies. This indicates that the fluid is relatively reduced during the retrograde skarn stage. Eu_N in Sch C precipitated in the quartz-sulfide stage is positively correlated with Eu^*_N. These scheelites exhibit significant negative Eu anomalies, implying that Eu mainly occurs as Eu^{3+}, and it reveals an oxidized condition.

The ratio of Eu^{3+}/Eu^{2+} in the fluid strongly controls the size of Eu anomaly even with negative Eu anomalies inherited from the initial hydrothermal fluid (Brugger et al., 2000). Therefore, europium anomaly in scheelite is widely used to directly reflect the redox state of ore-forming fluids (Song et al., 2014; Sun and Chen, 2017; Sun et al., 2019; Wu et al., 2019; Yuan et al., 2019). In addition to the redox condition, Eu anomalies of scheelite can be influenced by the modification by fluid-rock interaction, the pH of the fluid and the precipitation of Eu-rich minerals (Brugger et al., 2002, 2008; Sun et al., 2019; Liu et al., 2020). In the Sandaozhuang deposit, marbles of Sanchuan Formation without metasomatism exhibit weak negative Eu anomalies (Supplementary Table S4, δEu = 0.61–0.92). Interaction between hydrothermal fluids derived from granites with negative Eu anomalies and these rocks is unlikely to result in the positive Eu anomalies of Sch B. The water–rock reaction during skarn evolution is an equilibrium reaction and H_2CO_3 breaks down to H_2O and CO_2 ($H_2CO_3 \rightleftharpoons H_2O + CO_2\uparrow$) without an increase in H^+ (Tenno et al., 2018), while the fluid-carbonate reaction will certainly consume H^+ and therefore increase pH. Thus, the change in the Eu anomalies during the skarnization may also be related to the pH. In addition, it is difficult to determine the influence of common Ca-rich skarn minerals (such as garnet) on Eu anomaly in Sandaozhuang. Therefore, the Eu anomalies should be combined with other evidences to comprehensively reflect the change in redox state.

6.3.2. Redox condition indicated by Mo in scheelite

Molybdenum mainly occurs as Mo^{6+} under oxidizing conditions and Mo^{4+} in reduced environment. In the magmatic-hydrothermal systems, molybdenum is mainly transported as the oxidized Mo^{6+} form (Rempel et al., 2009). Mo^{6+} can substitute for W^{6+} to form a complete, albeit non-ideal solid solution series between scheelite ($CaWO_4$) and powellite ($CaMoO_4$) due to the similar valence states, ionic radii and coordination number (Hsu and Galli, 1973; Raimbault et al., 1993; Xu et al., 2019). However, Mo^{4+} combines with S^{2-} to form molybdenite (Song et al., 2014; Li et al., 2019; Liu et al., 2020). Therefore, in the process of molybdenite precipitation, the redox state must have been changed. Molybdenite and scheelite precipitate under similar temperature ranges, 600 – 200 °C and 500 – 200 °C, respectively (Cao, 1989; Wood and Samson, 2000). The variation of oxygen fugacity does not affect the precipitation of scheelite, but molybdenite tends to precipitate under the relatively reducing environment. Therefore, the variation of molybdenum content in scheelite show changes of physical and chemical conditions of ore-forming fluids in Sandaozhuang. Studies report that Mo content in scheelite from different deposits, is mainly controlled by three factors including: changing redox state (Song et al., 2014, 2019; Poulin et al., 2018; Sun et al., 2019); boiling process (Soloviev and Krivoschekov, 2011; Orhan, 2017; Liu et al., 2020); and evolving temperature (Zaw and Singoyi, 2000; Zhao et al., 2018; Song et al., 2019).

Low-fO_2 and high-fS_2 result in precipitation of nearly pure scheelite accompanied by molybdenite, whereas Mo-rich scheelite mainly precipitates under relatively high-fO_2 and low-fS_2 environment (Hsu and Galli 1973; Song et al., 2014; Poulin, 2016). Change of redox conditions affects valence state of molybdenum, reduced sulfur concentration and concentration of molybdenum in fluid, thus affecting the content of molybdenum in scheelite (Liu et al., 2020). The boiling process which leads to permeability increase and pressure decrease may promote the formation of Mo-rich scheelite at the early stage in oxidized W deposits and sulfide minerals at the late stage in reduced tungsten deposits (Kwak and Tan, 1981; Soloviev and Krivoschekov, 2011; Orhan, 2017). During boiling and vapor separation process, differential partitioning of H_2S and H_2 between the liquid phase and vapor phase may lead to the depletion of H_2S and increase of oxygen fugacity in the residual fluid (Cao, 1989; Jamtveit et al., 1993; Orhan, 2017; Liu et al., 2020). Reduction in temperatures affects Mo content in scheelite. For example, in Kara, Baoshan, Tasmania, and Kensu, Kyrgyzstan, the early relatively Mo-rich scheelite can precipitate at about 600 ℃, whereas late Mo-free scheelite formed at about 250 ℃ (Zaw and Singoyi, 2000; Song et al., 2019). Solubility curve of molybdenum decreases with decrease in temperature (Cao, 1989). Furthermore, fO_2 is closely related to temperature, and fO_2 can reduce by approximately 20 orders of magnitude from diagenetic temperature to 250 °C in porphyry deposits (Zhou, 1981; Wood and Samson, 2000; Liu et al., 2020). Furthermore, the earlier Mo-enriched minerals precipitation would significantly decrease Mo in fluids, resulting in low Mo content in the late generation scheelite. Due to the high partition coefficient of Mo between scheelite and fluids under oxidation condition, early scheelite would contain high Mo content so that the precipitation of Mo-rich scheelite/molybdenite would reduce Mo in fluids and in turn result in low-Mo scheelite in later generations.

Different types of scheelite from Sandaozhuang show a wide range of MoO_3 concentration (Fig. 8a), implying presence of the varying levels of substitution between Mo and W. The Mo contents of Sch A precipitated during the prograde skarn stage are significantly high, then decrease to Sch B precipitated in the retrograde skarn stage, Sch C formed in the late quartz-sulfide stage displays the lowest Mo contents (Fig. 10b and c). Previous microthermometry data show that fluid inclusions in the prograde diopside, garnet (394–552 °C; Shi et al., 2009) and retrograde stage quartz (347–458 °C; Weng et al., 2010) have similar homogenization temperatures during the skarn evolution stage. However, the decrease in temperature is an inevitable trend in the process of skarn evolution. The effect of temperature falling on Mo content in scheelite precipitated in the skarn period cannot be ignored. Fluid inclusions and $\delta^{13}C$-$\delta^{18}O$-δD isotopic studies report that the boiling process only occurs in the quartz-sulfide stage (Shi et al., 2009; Xiang et al., 2012b). Therefore, decreasing Mo concentrations from Sch A to Sch B is not related to the boiling process.

Petrographic evidence suggests that Mo mainly occurs as molybdenite during the retrograde skarn stage and the quartz-sulfide stage. Only a small proportion of molybdenite precipitated during the prograde

stage and coexisted with the relatively low-Mo Sch A-1. Therefore, the precipitation of Mo-rich scheelite and molybdenite in the early stage may have little effect on Sch B. In the retrograde skarn stage, amounts of Mo exist as molybdenite, and molybdenite coexist closely with Mo-poor Sch B (Fig. 7c-f). Mo contents decrease sharply from the early generation Sch A-2 to the late Sch B. These findings imply that Mo is partly released from the early generation Sch A-2 through a dissolution and reprecipitation process, and then secondary precipitates with original Mo in metallogenic fluid as molybdenite, showing a change from the oxidation to relative reduction of the ore-forming fluid. In addition, we find there is a detectable linear negative correlation between Eu anomalies and Mo concentration of scheelite during the skarn evolution in the Sandaozhuang deposit (Fig. 10c). The correlation shows that the redox states evaluated based on Mo content are consistent with those inferred from Eu anomaly. Redox categories of skarn deposits can be affected by country rocks (Meinert et al., 2005). Carbonaceous strata are widely distributed in Sandaozhuang, especially in the Meiyaogou Formation with stone coal interlayer larger than 150 m, and carbonaceous phyllite in Nannihu Formation and Sanchuan Formation (Shi et al., 2009). Therefore, the decrease in redox conditions from prograde stage to retrograde stage in Sandaozhuang may be caused by more involvement of carbonaceous carbonate wall rocks accompanied by decrease of temperature.

Fluid inclusions and $\delta^{13}C$-$\delta^{18}O$-δD isotopic studies have defined boiling process in the quartz-sulfide stage. Homogenization temperature of fluid inclusions in quartz-sulfide veins (~290 °C; Shi et al., 2009; Weng et al., 2010) is lower compared with that for skarn stage. Low temperature and boiling process result in high amount of molybdenite and other sulfides precipitating in this stage. Moreover, a large amount of molybdenum is already precipitated as molybdenite in the previous skarn stage, which can also capture a large amount of Mo in the fluid, resulting in low Mo content in the late Sch C. Compared with Sch B, the Mo content of Sch C does not decrease significantly (Fig. 10). It may be due to the increase of oxygen fugacity caused by the boiling process so that a part of Mo^{6+} will still be incorporated into Sch C.

In summary, the ore-forming process in Sandaozhuang changes from an oxidized Mo-rich-scheelite prograde stage to a reduced Mo-poor-scheelite retrograde stage. A considerable amount of molybdenum may first enter the early generation scheelite to form Mo-rich scheelite under the oxidized condition. With the decreasing of oxygen fugacity, partial molybdenum is released from the early generation scheelite and precipitates as molybdenite. The Mo-poor-scheelite in the quartz-sulfide stage is the end of W mineralization characterized by the low temperature and boiling process (Fig. 16).

6.3.3. *Redox condition indicated by compositions of clinopyroxene and garnet*

Tungsten skarn deposits can be generally subdivided into oxidation type and reduction type (Einaudi et al., 1981; Meinert et al., 2005). Mineral assemblages in "oxidized" W skarn deposits mainly consist of intermediate-Fe clinopyroxene ($Hd_{40–60}$), andraditic garnet ($And_{60–100}$) lacking a significant almandine component, and Mo-rich scheelite. On the contrary, "reduced" W skarns contain hedenbergitic clinopyroxene ($Hd_{70–95}$), garnet ($And_{10–30}$) containing at least 20% spessartine + almandine component, and Mo-poor scheelite (Einaudi et al., 1981; Newberry, 1998; Zhao et al., 2018).

The Sandaozhuang deposit is characterized by Mg-rich clinopyroxene ($Di_{40-81}Hd_{17-47}$), grossularite–andradite ($And_{22–89}Gro_{6-77}$) and Mo-rich scheelite (up to 24.45%) (Fig. 8b, Fig. 13a and b). The main skarn mineral assemblage implies that it can be broadly divided into an oxidized tungsten deposit, which is more similar to oxidized tungsten skarns at Jitoushan and Baizhangyan deposit in South China (Song, 2010), Kara deposit in Australia (Zaw and Singoyi, 2000) and King Island (Kwak and Tan, 1981). These skarn minerals are mainly precipitated in the prograde skarn stage, therefore, it may only indicate the oxidized conditions during the prograde stage.

In addition, Sch A-2 with high Mo contents coexisting with Fe-enrich andradite (Fig. 6d), and minor Sch A-1 with relatively lower Mo content coexisting with Al-enrich grossular (Gro_{70-77}And22–29) precipitated in the prograde stage (Fig. 6a). A small amount of molybdenite is also observed in such oxidized prograde stage (Fig. 6b, c), and it coexists with Sch A-1, implying a lower fO_2 environment. The minor molybdenite can

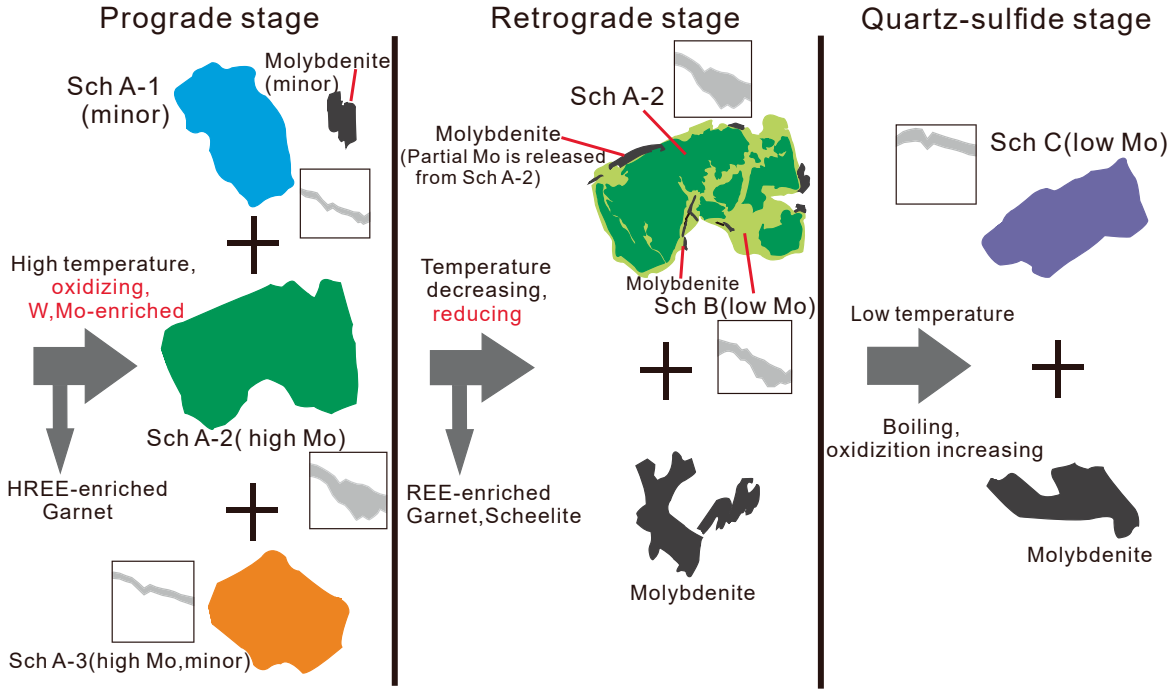

Fig. 16. The evolution model of W-Mo mineralization process in the Sandaozhuang deposit.

be attributed to the interaction between initial weak oxidized ore-forming fluids with the surrounding rock, thus changing the fluids to a reduced state, and consumption of H^+ when the fluid reacts with wollastonite and calcite (Xiang et al., 2016). Therefore, molybdenite precipitated when the concentration of Mo^{4+} and S^{2-} are sufficient, implying a high concentration of Mo in the primary ore-forming fluid. Notably, in a single isolated garnet precipitated in the late prograde skarn stage, the concentration of grossularite from the core to rim increases gradually, whereas the concentration of andradite decreases gradually (Fig. 13c and d). This may also confirm that the oxygen fugacity gradually decreases during the evolution from late prograde stage to retrograde stage.

7. Conclusion

(1) Ore-forming materials in the Sandaozhuang W-Mo deposit were mainly derived from the Nannihu granite porphyry. The intense fluid-rock interaction may also extract some metals from the country rocks, especially calcium, which promotes the large-scale tungsten mineralization in the Sandaozhuang deposit.

(2) The various Mo contents in the three generations of scheelite reflect changes in the redox state of the ore-forming fluid. According to the valence state changes of Eu in scheelite, and composition of garnet and clinopyroxene, we propose that the ore-forming fluid changes from an oxidized to a reduced state in the skarn stage and then to an oxidized state in the quartz-sulfide stage.

(3) Three molybdenum precipitation events are identified in the Sandaozhuang deposit. The first one shows that a high concentration of Mo in the primary ore-forming fluid meets the local reduction environment in the prograde stage. The second shows that the change from oxidation to reduction of the ore-forming fluid in the retrograde stage, where partial Mo is released from early generation scheelite crystals and occurs as molybdenite. The last event reflects fluid cooling and boiling process in the late quartz-sulfide stage.

Declaration of Competing Interest

The authors declare that they have no known competing financial interests or personal relationships that could have appeared to influence the work reported in this paper.

Acknowledgments

This work was supported by the National Natural Science Foundation of China (Grant Nos. 41872088 & 92062102). We thank Jiangwei Han, Shiyan Wang and Jianmin Yang for field assistance. We highly appreciate Xiaochun Li and Alexandra Yang Yang for their helpful suggestions and language improvement on drafts of the manuscript. We are also very grateful to Editor-in-Chief Huayong Chen, Associated Editor Qingfei Wang, M. Santosh, and three anonymous reviewers for their constructive comments that lead to significant improvement of the manuscript. This is contribution No.IS-3095 from GIGCAS.

Appendix A. Supplementary data

Supplementary data to this article can be found online at https://doi.org/10.1016/j.oregeorev.2021.104551.

References

Bao, Z., Wang, C.Y., Zhao, T., Li, C., Gao, X., 2014. Petrogenesis of the Mesozoic granites and Mo mineralization of the Luanchuan ore field in the East Qinling Mo mineralization belt. Central China. Ore Geol. Rev. 57, 132–153.

Bao, Z.W., Zeng, Q.S., Zhao, T.P., Yuan, Z.L., 2009. Geochemistry and petrogenesis of the ore-related Nannihu and Shangfanggou granite porphyries from east Qinling belt of molybdenum mineralization. Acta Petrol. Sin. 25, 2523–2536 (in Chinese with English abstract).

Bau, M., 1996. Controls on the fractionation of isovalent trace elements in magmatic and aqueous systems: evidence from Y/Ho, Zr/Hf, and lanthanide tetrad effect. Contrib. Mineral. Petrol. 123 (3), 323–333.

Bau, M., Dulski, P., 1995. Comparative study of yttrium and rare-earth element behaviours in fluorine-rich hydrothermal fluids. Contrib. Mineral. Petrol. 119 (2-3), 213–223.

Bell, K., Anglin, C.D., Franklin, J.M., 1989. Sm-Nd and Rb-Sr isotope systematics of scheelites: possible implications for the age and genesis of vein-hosted gold deposits. Geology 17 (6), 500. https://doi.org/10.1130/0091-7613(1989)017<0500:SNARSI>2.3.CO;2.

Blundy, J., Wood, B., 1994. Prediction of crystal-melt partition coefficients from elastic moduli. Nature 372 (6505), 452–454.

Brugger, J., Bettiol, A.A., Costa, S., Lahaye, Y., Bateman, R., Lambert, D.D., Jamieson, D. N., 2000. Mapping REE distribution in scheelite using luminescence. Mineral. Mag. 64 (5), 891–903.

Brugger, J., Etschmann, B., Pownceby, M., Liu, W., Grundler, P., Brewe, D., 2008. Oxidation state of europium in scheelite: tracking fluid-rock interaction in gold deposits. Chem. Geol. 257 (1-2), 26–33.

Brugger, J., Maas, R., Lahaye, Y., McRae, C., Ghaderi, M., Costa, S., Lambert, D., Bateman, R., Prince, K., 2002. Origins of Nd–Sr–Pb isotopic variations in single scheelite grains from Archaean gold deposits Western Australia. Chem. Geol. 182 (2-4), 203–225.

Burt, D.M., 1989. Compositional and phase relations among rare earth elements. Rev. Mineral. 21, 259–307.

Cao, X.Y., 1989. Solubility of molybdenite and the transport of molybdenum in hydrothermal solutions. Ph. D'.s thesis. Iowa State University, the United States of America, pp. 1–111.

Chang, Z., Shu, Q., Meinert, L.D., 2019. Skarn deposits of China: Society of Economic Geologists. Special Publication 22, 189–234.

Chen, Y., Li, C., Zhang, J., Li, Z., Wang, H., 2000. Sr and O isotopic characteristics of porphyries in the Qinling molybdenum deposit belt and their implication to genetic mechanism and type. Sci. China Ser. D Earth Sci. 43 (S1), 82–94.

Chen, Y.-J., Pirajno, F., Sui, Y.-H., 2004. Isotope geochemistry of the Tieluping silver-lead deposit, Henan, China: a case study of orogenic silver-dominated deposits and related tectonic setting. Mineral. Depos. 39 (5-6), 560–575.

Cottrant, J.F., 1981. Cristallochimie et géochimie des terres rares dans la scheelite: Application à quelques gisements francais. Ph.D. thesis. University of Paris-VI, France.

Darbyshire, D.P.F., Pitfield, P.E.J., Campbell, S.D.G., 1996. Late Archean and Early Proterozoic gold-tungsten mineralization in the Zimbabwe Archean craton: Rb-Sr and Sm-Nd isotope constraints. Geology 24 (1), 19. https://doi.org/10.1130/0091-7613(1996)024<0019:LAAEPG>2.3.CO;2.

Deer, W.A., Howie, R.A., Zussman, J., 1966. An Introduction to the Rock Forming Minerals. Longman Press, New York, p. 515.

Ding, T., Ma, D., Lu, J., Zhang, R., 2018. Garnet and scheelite as indicators of multistage tungsten mineralization in the Huangshaping deposit, southern Hunan province. China. Ore Geol. Rev. 94, 193–211.

Dostal, J., Kontak, D.J., Chatterjee, A.K., 2009. Trace element geochemistry of scheelite and rutile from metaturbidite-hosted quartz vein gold deposits Meguma Terrane, Nova Scotia, Canada: genetic implications. Mineral. Petrol. 97 (1-2), 95–109.

Eichhorn, R., Holl, R., Jagoutz, E., Schrer, U., 1997. Dating scheelite stages: a strontium, neodymium, lead approach from the Felbertal tungsten deposit, Central Alps. Austria. Geochim. Cosmochim. Acta 61, 5005–5022.

Einaudi, M.T., Meinert, L.D., Newberry, R.J., 1981. Skarn deposits. Econ. Geol. 75, 317–391.

Enami, M., Cong Bolin, Yoshida, T., Kawabe, I., 1995. A mechanism for Na incorporation in garnet: an example from garnet in orthogneiss from the Su-Lu terrane, eastern China. Am. Mineral. 80 (5-6), 475–482.

Geological Survey Team 1 of Henan Bureau of Geology, 1980. Exploration Report of the Sandaozhuang Mo-W deposit, Luanchuan County, Henan Province. (in Chinese).

Ghaderi, M., Palin, J.M., Campbell, I.H., Sylvester, P.J., 1999. Rare earth element systematics in scheelite from hydrothermal gold deposits in the Kalgoorlie-Norseman region, Western Australia. Econ. Geol. 94, 423–437.

Green, T.H., Pearson, N.J., 1983. Effect of pressure on rare earth element partition coefficients in common magmas. Nature 305 (5933), 414–416.

Guo, S., Chen, Y.i., Liu, C.-Z., Wang, J.-G., Su, B., Gao, Y.-J., Wu, F.-Y., Sein, K., Yang, Y.-H., Mao, Q., 2016. Scheelite and coexisting F-rich zoned garnet, vesuvianite, fluorite, and apatite in calc-silicate rocks from the Mogok metamorphic belt, Myanmar: Implications for metasomatism in marble and the role of halogens in W mobilization and mineralization. J. Asian. Earth. Sci. 117, 82–106.

Han, J.W., Guo, B., Wang, H.W., Ma, Y.H., Feng, Z.K., Yun, H., Yan, C.H., Li, D., 2015. Geochemistry of the Xiyuku large concealed porphyry Mo–W ore deposit. Luanchuan Country. Acta Petro. Sin. 31, 1789–1796 (in Chinese with English abstract).

Han, J.S., Chen, H.Y., Hong, W., Hollings, P., Chu, G.B., Zhang, L., Sun, S.Q., 2020. Texture and geochemistry of multi-stage hydrothermal scheelite in the Tongshankou porphyry-skarn Cu-Mo(-W) deposit, eastern China: Implications for ore-forming process and fluid metasomatism. Am. Mineral. 105, 945–954.

Hellstrom, J., Paton, C., Woodhead, J., Hergt, J., 2008. Iolite: software for spatially resolved LA-(quad and MC) ICPMS analysis. Short Course Ser. - Mineral. Assoc. Can. 40, 343–348.

Hsu, L.C., Galli, P.E., 1973. Origin of the scheelite-powellite series of minerals. Econ. Geol. 68, 681–696.

Huang, D.H., Wu, C.Y., Du, A.D., He, H.L., 1995. Re–Os isotope ags of molybdenum deposits in East Qinling and their significance. Chin. J. Geochem. 14, 313–322.

Jaffe, H.W., 1951. The role of yttrium and other minor elements in the garnet group. Am. Mineral. 36, 133–155.

Jamtveit, B., Wogelius, R.A., Fraser, D.G., 1993. Zonation patterns of skarn garnets: records of hydrothermal system evolution. Geology 21 (2), 113. https://doi.org/10.1130/0091-7613(1993)021<0113:ZPOSGR>2.3.CO;2.
Jin, C., Gao, X.-Y., Chen, W.T., Zhao, T.-P., 2018. Magmatic-hydrothermal evolution of the Donggou porphyry Mo deposit at the southern margin of the North China Craton: evidence from chemistry of biotite. Ore Geol. Rev. 92, 84–96.
Kempe, U., Belyatsky, B., Krymsky, R., Kremenetsky, A., Ivanov, P., 2001. Sm-Nd and Sr isotope systematics of scheelite from the giant Au (-W) deposit Muruntau (Uzbekistan): implications for the age sources of Au mineralization. Miner. Deposita 36, 379–392.
Kent, A.J.R., Campbell, I.H., McCulloch, M.T., 1995. Sm-Nd systematics of hydrothermal scheelite from the Mount Charlotte mine, Kalgoorlie, Western Australia: an isotopic link between gold mineralization and komatiites. Econ. Geol. 90, 2329–2335.
Kröner, A., Compston, W., Guo-wei, Z., An-lin, G., Todt, W., 1988. Age and tectonic setting of Late Archean greenstone-gneiss terrain in Henan Province, China, as revealed by single-grain zircon dating. Geology 16 (3), 211. https://doi.org/10.1130/0091-7613(1988)016<0211:AATSOL>2.3.CO;2.
Kwak, T.A.P., Tan, T.H., 1981. The geochemistry of zoning in skarn minerals at the King Island (Dolphin) Mine. Econ. Geol. 76, 468–497.
Li, J., Li, X., Xiao, R., 2019. Multiple-stage tungsten mineralization in the Silurian Jiepai W skarn deposit, South China: insights from cathodoluminescence images, trace elements, and fluid inclusions of scheelite. J. Asian Earth Sci. 181, 103898. https://doi.org/10.1016/j.jseaes.2019.103898.
Li, J.-W., Bi, S.-J., Selby, D., Chen, L., Vasconcelos, P., Thiede, D., Zhou, M.-F., Zhao, X.-F., Li, Z.-K., Qiu, H.-N., 2012. Giant Mesozoic gold provinces related to the destruction of the North China Craton. Earth Planet. Sci. Lett. 349-350, 26–37.
Li, X.-Y., Gao, J.-F., Zhang, R.-Q., Lu, J.-J., Chen, W.-H., Wu, J.-W., 2018. Origin of the Muguayuan veinlet-disseminated tungsten deposit, South China Constraints from in-situ trace element analyses of scheelite. Ore Geol. Rev. 99, 180–194.
Li, Y.F., Mao, J.W., Bai, F.J., Li, J.P., He, Z.J., 2003. Re–Os isotopic dating of molybdenites in the Nannihu molybdenum (tungsten) orefield in the Eastern Qinling and its geological significance. Geol. Rev. 49, 652–659 (in Chinese with English abstract).
Liu, B., Li, H., Wu, Q.-H., Evans, N.J., Cao, J.-Y., Jiang, J.-B., Wu, J.-H., 2019. Fluid evolution of Triassic and Jurassic W mineralization in the Xitian ore field, South China: constraints from scheelite geochemistry and microthermometry. Lithos 330-331, 1–15.
Liu, S.-L., Hu, F.-F., Fan, H.-R., Yang, K.-F., Qiu, Z.-J., Hu, H.-L., 2020. Ore-forming processes in the Xingjiashan W-Mo skarn deposit (Jiaodong, China): Insights from multi-generation scheelite and garnet geochemistry. Ore Geol. Rev. 124, 103645. https://doi.org/10.1016/j.oregeorev.2020.103645.
Liu, Y., Hu, Z., Gao, S., Günther, D., Xu, J., Gao, C., Chen, H., 2008. In situ analysis of major and trace elements of anhydrous minerals by LA-ICP-MS without applying an internal standard. Chem. Geol. 257 (1-2), 34–43.
Mao, J.W., Pirajno, F., Xiang, J.F., Gao, J.J., Ye, H.S., Li, Y.F., Guo, B.J., 2011. Mesozoic molybdenum deposits in the east Qinling-Dabie orogenic belt: characteristics and tectonic settings. Ore Geol. Rev. 43 (1), 264–293.
Mao, J.W., Xie, G.Q., Bierlein, F., Qü, W.J., Du, A.D., Ye, H.S., Pirajno, F., Li, H.M., Guo, B.J., Li, Y.F., Yang, Z.Q., 2008. Tectonic implications from Re–Os dating of Mesozoic molybdenum deposits in the East Qinling-Dabie orogenic belt. Geochim. Cosmochim. Acta 72 (18), 4607–4626.
Mao, J.-W., Xie, G.-Q., Pirajno, F., Ye, H.-S., Wang, Y.-B., Li, Y.-F., Xiang, J.-F., Zhao, H.-J., 2010. Late Jurassic-Early Cretaceous granitoid magmatism in Eastern Qinling, central-eastern China: SHRIMP zircon U-Pb ages and tectonic implications. Aust. J. Earth Sci. 57 (1), 51–78.
Mao, J., Xiong, B., Liu, J., Pirajno, F., Cheng, Y., Ye, H., Song, S., Dai, P., 2017. Molybdenite Re/Os dating, zircon U-Pb age and geochemistry of granitoids in the Yangchuling porphyry W-Mo deposit (Jiangnan tungsten ore belt), China: implications for petrogenesis, mineralization and geodynamic setting. Lithos 286-287, 35–52.
McDonough, W.F., Sun, S.-s., 1995. The composition of the Earth. Chem. Geol. 120 (3-4), 223–253.
Meinert, L.D., Dipple, G.M., Nicolescu, S., 2005. World skarn deposits. Economic Geology 100th Anniversary 299–336.
Mueller, A.G., Laeter, J.R.D., David, I., Groves, D.I., 1991. Strontium Isotope Systematics of Hydrothermal Minerals from Epigenetic Archean Gold Deposits in the Yilgarn Block, Western Australia. Econ. Geol. 86, 780–809.
Nassau, K., Loiacono, G.M., 1963. Calcium tungstate-III: trivalent rare earth substitution. J. Phys. Chem. Solids 24 (12), 1503–1510.
Newberry, R.J., 1982. Tungsten-bearing skarns of the Sierra Nevada; I, The Pine Creek mine, California. Econ. Geol. 77, 823–844.
Newberry, R.J., 1998. W-and Sn-skarn deposits: a 1998 status report. In: Lentz, D.R. (Ed.), Mineralized Intrusion-Related Skarn Systems. Mineralogical Association of Canada, Ottawa, pp. 289–335.
Noble, S., Spooner, E.T.C., Harris, F., 1984. The Logtung large tonnage, low-grade W (scheelite)-Mo porphyry deposit, south-central Yunkon Territory. Econ. Geol. 79, 848–868.
Orhan, A., 2017. Evolution of the Mo-rich scheelite skarn mineralization at Kozbudaklar, Western Anatolia, Turkey: evidence from mineral chemistry and fluid inclusions. Ore Geol. Rev. 80, 141–165.
Paton, C., Hellstrom, J., Paul, B., Woodhead, J., Hergt, J., 2011. Iolite: Freeware for the visualization and processing of mass spectrometric data. J. Anal. At. Spectrom. 26, 2508–2518.
Peng, J.T., Hu, R.Z., Zhao, J.H., Fu, Y.Z., 2003. Scheelite Sm-Nd dating and quartz Ar-Ar dating from Woxi Au-Sb-W deposit western Hunan. Chin. Sci. Bull. 48, 2640–2646 (in Chinese with English abs.).
Polya, D.A., 1988. Efficiency of hydrothermal ore formation and the Panasqueira W-Cu (Ag)-Sn vein deposit. Nature 333 (6176), 838–841.
Poulin, R.S., 2016. A study of the crystal chemistry, cathodoluminescence, geochemistry, oxygen isotopes in scheelite: application towards discriminating among different ore-deposit systems. Master's thesis. Laurentian University, Sudbury, Canada, pp. 1–284.
Poulin, R.S., Kontak, D.J., Andrew, M.A., Beth, M., Mcclenaghan, B.M., 2018. Assessing Scheelite As an Ore-deposit Discriminator Using Its Trace-element REE Chemistry. Can. Mineral. 56 (3), 265–302.
Qi, J.P., Song, Y.W., Li, S.Q., Chen, F.K., 2009. Single-grain Rb-Sr isotopic composition of the Xigou Pb-Zn-Ag deposit, Luanchuan. Henan province. Acta Petrol. Sin. 25, 2843–2854 (in Chinese with English abstract).
Raimbault, L., Baumer, A., Dubru, M., Benkerrou, C., Croze, V., Zahm, A., 1993. REE fractionation between scheelite and apatite in hydrothermal conditions. Am. Mineral. 78, 1275–1285.
Rempel, K.U., Williams-Jones, A.E., Migdisov, A.A., 2009. The partitioning of molybdenum (VI) between aqueous liquid and vapour at temperatures up to 370 C. Geochim. Cosmochim. Acta 73 (11), 3381–3392.
Sato, K., 1980. Tungsten skarn deposit of the Fujigatani mine, southwest Japan. Econ. Geol. 75, 1066–1082.
Shannon, R.D., 1976. Revised effective ionic radii and systematic studies of interatomic distances in halides and chalcogenides. Acta Crystallogr. Sect. A 32 (5), 751–767.
Shi, Y.X., Li, N., Yang, Y., 2009. Ore geology and fluid inclusion geochemistry of the Sandaozhuang Mo–W deposit in Luanchuan County. Henan Province. Acta Petrol. Sin. 25, 2575–2587 (in Chinese with English abstract).
Soloviev, S.G., 2015. Geology, mineralization, and fluid inclusion characteristics of the Kumbel oxidized W-Cu–Mo skarn and Au–W stockwork deposit in Kyrgyzstan. Tien Shan. Miner. Deposita 50 (2), 187–220.
Soloviev, S.G., Krivoschekov, N.N., 2011. Petrochemistry of Rocks in the Chorukh-Dairon Monzonite-Syenite-Granite Pluton, Northern Tajikistan. Geochem. Int. 49 (7), 691–710.
Song, G.X., 2010. Research on Magmatism-Mineralization and Metallogenic system of skarn-porphyry type W-Mo deposits in Chizhou area, the Middle-Lower Yangtze Valley. Ph.D. thesis. Institute of Geology and Geophysics, Chinese Academy of Sciences.
Song, G., Cook, N.J., Li, G., Qin, K., Ciobanu, C.L., Yang, Y., Xu, Y., 2019. Scheelite geochemistry in porphyry-skarn W-Mo systems: a case study from the Gaojiabang Deposit. East China. Ore Geol. Rev. 113, 103084. https://doi.org/10.1016/j.oregeorev.2019.103084.
Song, G., Qin, K., Li, G., Evans, N.J., Chen, L., 2014. Scheelite elemental and isotopic signatures: implications for the genesis of skarn-type W-Mo deposits in the Chizhou Area, Anhui Province, Eastern China. Am. Mineral. 99 (2-3), 303–317.
Su, S.Q., Qin, K.Z., Li, G.M., Olin, P., Thompson, J., 2019. Cathodoluminescence and trace elements of scheelite: constraints on ore-forming processes of the Dabaoshan porphyry Mo-W deposit, South China. Ore Geol. Rev. 103183.
Sun, K.K., Chen, B., 2017. Trace elements and Sr-Nd isotopes of scheelite: implications for the W-Cu-Mo polymetallic mineralization of the Shimensi deposit, South China. Am. Mineral. 102, 1114–1128.
Sun, K., Chen, B., Deng, J., 2019. Ore genesis of the Zhuxi supergiant W-Cu skarn polymetallic deposit, South China: evidence from scheelite geochemistry. Ore Geol. Rev. 107, 14–29.
Sun, Y., Ren, X., 1986. Ore minerals in Shizhuyuan deposit. Acta Mineralogica Sinica 2, 179–187 (in Chinese with English abstract).
Tenno, T., Rikmann, E., Uiga, K., Zekker, I., Mashirin, A., Tenno, T., 2018. A novel proton transfer model of the closed equilibrium system H2O-CO2-CaCO3-NHx. In: Proceedings of the Estonian Academy of Sciences, pp. 260–270.
Tomschi, H.P., Oberthür, T., Saager, R., and Kramers, J., 1986, Geochemical and mineralogical data on the genesis of the Mazowe gold field in the Harare Bindura greenstone belt, Zimbabwe [ext. abs]: Geocongress'86, Johannesburg, South Africa 1986, Extended Abstracts, 345–348.
Van Orman, J.A., Grove, T.L., Shimizu, N., 2001. Rare earth element diffusion in diopside: influence of temperature, pressure, and ionic radius and an elasticmodel for diffusion in silicates. Contrib. Miner. Petrol. 141 (6), 687–703.
Voicu, G., Bardoux, M., Stevenson, R., Jébrak, M., 2000. Nd and Sr isotope study of hydrothermal scheelite and host rocks at Omai, Guiana Shield: implications for ore fluid source and flow path during the formation of orogenic gold deposits. Miner. Deposita 35 (4), 302–314.
Wang, X., Wang, X., Sun, C., 2010. REE geochemistry of scheelite and Sm-Nd dating for the Houchangchuan scheelite deposit in Gansu. Miner. Deposits 30 (1), 64–68 (in Chinese with English abstract).
Weng, J.C., Pan, J.Z., Li, W.Z., Wang, H.J., 2010. Ore material composition and ore-forming stage division of the Sandaozhuang superlarge molybdenum-tungsten ore deposit in Luanchuan. Geophys. Geochem. Explor. 34, 170–175.
Wood, S.A., Samson, I.M., 2000. The hydrothermal geochemistry of tungsten in granitoid environments: I. Relative solubilities of ferberite and scheelite as a function of T, P, pH, and m NaCl. Econ. Geol. 95 (1), 143–182.
Wu, S., Mao, J., Ireland, T.R., Zhao, Z., Yao, F., Yang, Y., Sun, W., 2019. Comparative geochemical study of scheelite from the Shizhuyuan and Xianglushan tungsten skarn deposits, South China: implications for scheelite mineralization. Ore Geol. Rev. 109, 448–464.
Xiang, J.F., Mao, J.W., Pei, R.F., Ye, H.S., Wang, C.Y., Tian, Z.H., Wang, H.L., 2012a. New geochronological data of granites and ores from the Nannihu-Sandaozhuang Mo (W) deposit. Geol. China. 39, 458–473 (in Chinese with English abstract).
Xiang, J.F., Pei, R.F., Xing, B., Wang, C.Y., Tian, Z.H., Chen, X.D., Ye, H.S., Wang, H.L., 2016. The formation process and Mo (W) mineralizaton of the skarn in the

Nannihu−Sandaozhuang Mo (W) deposit. Geol. China. 43, 2131–2153 (in Chinese with English abstract).
Xiang, J.F., Pei, R.F., Ye, H.S., Wang, C.Y., Tian, Z.H., 2012b. Source and evolution of the ore-forming fluid in the Nannihu-Sandaozhuang Mo (W) deposit: Constraints from C-H-O stable isotope data. Geol. China. 39, 1778–1788 (in Chinese with English abstract).
Xiao, Z.J., Sun, W.Z., 2007. Ore-forming Conditions and Prospecting of the Yechangping Mo-W Deposit in Lushi County, Henan Province. Geol. Surv. Res. 30, 141–148 (in Chinese with English abstract).
Xie, G., Mao, J., Bagas, L., Fu, B., Zhang, Z., 2019. Mineralogy and titanite geochronology of the Caojiaba W deposit, Xiangzhong metallogenic province, southern China: implications for a distal reduced skarn W formation. Miner. Deposita 54 (3), 459–472.
Xiong, D.X., Sun, X.M., Shi, G.Y., Wang, S.W., Gao, J.F., Xue, T., 2006. Trace elements, rare earth elements (REE) and Nd-Sr isotopic compositions in scheelites and their implications for the mineralization in Daping gold mine in Yunnan province. China. Acta Petrol. Sin. 22, 733–741 (in Chinese with English abstract).
Xu, J., Ciobanu, C.L., Cook, N.J., Slattery, A., 2019. Crystals from the powellite-scheelite series at the nanoscale: a case study from the Zhibula Cu Skarn. Gangdese Belt. Tibet. Minerals 9, 340–362.
Yang, Y.-F., Li, N., Chen, Y.-J., 2012. Fluid inclusion study of the Nannihu giant porphyry Mo–W deposit, Henan Province, China: Implications for the nature of porphyry ore-fluid systems formed in a continental collision setting. Ore Geol. Rev. 46, 83–94.
Yang, Y.F., Li, N., Yang, Y., 2009. Fluid inclusion study of the Nannihu porphyry Mo–W deposit, Luanchuan country. Henan Province. Acta Petrol. Sin. 25, 2550–2562 (in Chinese with English abstract).
Yu, P., 2012. The research on the mineralogical characteristics of tungsten deposit in Pangushan, Jiangxi. M.Sc. thesis. Chang' an University, p. 83.
Yuan, L., Chi, G., Wang, M., Li, Z., Xu, D., Deng, T., Geng, J., Hu, M., Zhang, L., 2019. Characteristics of REEs and trace elements in scheelite from the Zhuxi W deposit, South China: Implications for the ore-forming conditions and processes. Ore Geol. Rev. 109, 585–597.
Zaw, K., Singoyi, B., 2000. Formation of magnetite-scheelite skarn mineralization at Kara, northwestern Tasmania: evidence from mineral chemistry and stable isotopes. Econ. Geol. 95, 1215–1230.
Zhang, G.W., Guo, A.L., Liu, F.T., Xiao, Q.H., Meng, Q.R., 1996. Three-dimensional architecture and dynamic analysis of the Qinling orogenic belt. Sci. China Ser. D-Earth Sci. 26, 1–6.
Zhao, T., Zhai, M., Xia, B., Li, H., Zhang, Y., Wan, Y., 2004. Zircon U-Pb SHRIMP dating for the volcanic rocks of the Xiong'er Group: Constraints on the initial formation age of the cover of the North China Craton. Chin. Sci. Bull. 49 (23), 2495–2502.
Zhao, W.W., Zhou, M.-F., Williams-Jones, A.E., Zhao, Z., 2018. Constraints on the uptake of REE by scheelite in the Baoshan tungsten skarn deposit, South China. Chem. Geol. 477, 123–136.
Zhou, X.R., 1981. Estimation of oxygen fugacity and its application in petrology. Geol. Explor. 11, 40–48 (in Chinese).